International Journal of Thermal Sciences 197 (2024) 108823

Contents lists available at ScienceDirect

International Journal of Thermal Sciences

journal homepage: www.elsevier.com/locate/ijts

A hybrid slot jet impingement/microchannel heat sink for cooling high-power electronic devices: A combined experimental and numerical study

H.C. Cui, Z.K. Zhang, M.J. Yu, Z.C. Liu, W. Liu *

School of Energy and Power Engineering, Huazhong University of Science and Technology, Wuhan, 430074, China

ARTICLE INFO

Keywords:
Hybrid heat sink
Slot jet impingement
Microchannel
Numerical simulation and experiment

ABSTRACT

Jet impingement cooling and microchannel cooling have been extensively adopted as the efficient cooling technologies in the thermal management of high-power electronics. In this research, an optimal hybrid slot jet impingement/microchannel heat sink, integrating the merits of two cooling methods, obtained from multi-objective optimization is machined and tested experimentally. By varying test conditions, the impact of inlet mass flow rate, inlet temperature and heat flux variations on the flow resistance and heat removal capacity of the optimal heat sink are investigated. Moreover, by conducting overall 3D numerical simulation, the internal flow and heat transfer behaviours of the heat sink are also investigated. By analyzing the flow field inside the heat sink, the experimental phenomena are interpreted. Comparing the relative errors between the numerical simulation and experimental measurement values under the same working conditions, it could be observed that the maximum relative error of the pressure drop is about 9.7 %, and the maximum relative error of the average temperature of the heated surface is only 0.9 %. According to the experimental results, as the heat flux is 200 W/cm^2, the inlet temperature is 293 K and the inlet mass flow rate is 28 g/s, the average temperature of the heated surface does not surpass 348 K, while the pressure drop is only 2.46 kPa. Additionally, compared with the literature results, the hybrid heat sink obtained after multi-objective optimization in this study realizes a significant enhancement in cooling capacity, while the pumping power to heating power ratio is not significantly increased.

1. Introduction

With striking breakthroughs of artificial intelligence (AI) technology in computer vision [1,2], speech recognition [3,4] and natural language processing [5], AI is gradually becoming an indispensable part of people's lives and bringing great convenience to their lives. The rapid development and breakthroughs in the field of artificial intelligence can largely be attributed to the exponential growth in computing power of semiconductor chips [6]. For example, compared with the first popularized deep learning model in 2012, i.e. AlexNet [7], one of the largest models, i.e. GPT-3 [8], issued in 2020, requires 600,000 times the computing power [9]. In order to cope with the continuous development of AI, the demand for processing massive data on the chip's arithmetic power requirements is increasingly high. Under the current chip design strategy, one of the effective ways to enhance the chip's computing power is to reduce the transistor size and increase the transistor density, which will increase the power consumption and result in an increased heat generation. According to the available literature, the heat flux of some conventional ICs has reached 100 W/cm^2 [10]. In the foreseeable future, it could be anticipated that the heat flux generated in 3D stacked chips will exceed 1000 W/cm^2 [11]. In the face of such high heat flux, the use of some conventional cooling technologies can barely guarantee that the chip works efficiently within a safe temperature range [12]. As a result, investigating cooling technologies that are more efficient, stable and have higher heat dissipation capability is extremely momentous to the sustainable and rapid development of semiconductor devices [13,14]. Compared with conventional cooling technologies, jet impingement cooling technology and microchannel cooling technology have become hot research topics in recent years because of its outstanding heat transfer performance, and are considered to be the main solutions for heat removal of high-power electronics in the future.

The conception of microchannel cooling was first introduced by Tuckerman and Pease et al. [15] and successfully applied to the very

* Corresponding author.
E-mail address: w_liu@hust.edu.cn (W. Liu).

https://doi.org/10.1016/j.ijthermalsci.2023.108823
Received 28 August 2023; Received in revised form 7 November 2023; Accepted 29 November 2023
Available online 11 December 2023

Nomenclature

A	heated surface area (mm^2)
H	height (mm)
h	heat transfer coefficient ($W{\cdot}cm^{-2}{\cdot}K^{-1}$)
k	turbulence kinetic energy (J)
L	length (mm)
$\dot{m}$	mass flow rate of the coolant ($g{\cdot}s^{-1}$)
P	pressure drop (Pa)
Q	heating power of the heat source (W)
q	heat flux of the heated surface ($W{\cdot}cm^{-2}$)
T	temperature (K)
$\dot{V}$	coolant volume flow rate ($L{\cdot}min^{-1}$)
W	width (mm) or the pumping/heating power (W)
x, y, z	orthogonal coordinate system

Greek symbols

ε	dissipation rate of turbulence kinetic energy
λ	thermal conductivity ($W{\cdot}m^{-1}{\cdot}K^{-1}$)
φ	channel width ratio

Subscript

ave	the average value
f	average value of inlet and outlet
heat	heated surface
heating	heating power
hs	heat sink
in	heat sink inlet or inlet branch passage
nc	natural convection
out	heat sink outlet or the outlet branch passage
pumping	the pumping power
s	solid domain
test	experimental test
trans	heat transfer surface

Abbreviations

AI	artificial intelligence
DC	direct current
GPT-3	Generative Pre-trained Transformer 3
ICs	integrated circuits
JIMHS	jet impingement/microchannel heat sink
PEEK	polyether-ether-ketone
SJIMHS	slot jet impingement/microchannel heat sink
VLSI	very large scale integration

large scale integration (VLSI) circuit. The outstanding performance of the microchannel cooling technology has motivated scholars at home and abroad to perform a number of numerical simulations and experimental studies to further improve its thermal-hydraulic performance. These studies have focused on novel structural designs and key structural parameters, such as the number of microchannel layers [16–18], channel size [19], channel shape [20,21] and disturbance structures [22,23]. Although the advantages, such as large specific surface area and compactness, make microchannel heat sink ideal for cooling highly integrated electronic devices, large pressure and temperature gradients along the flow path are the main barriers restricting its application [24].

Different from the microchannel cooling, jet impingement cooling relies on the high-speed fluid vertically scouring the bottom surface to significantly enhance the heat removal capacity. Jet impingement can significantly enhance fluid disturbance within the heat sink, attenuate boundary layer growth, and enhance the heat and momentum exchange between fluids [25]. Similar to microchannel cooling technology, jet impingement cooling technology has also become a research hotspot in recent years due to its unique advantages, and the researches mainly focus on the jet hole size [26,27], jet hole shape [28,29], jet hole placement pattern [30], jet hole number [31] and jet-to-target spacing [32,33]. However, for traditional jet array impingement heat sink, although higher heat transfer coefficient and lower pressure drop could be achieved, the heat transfer coefficient distribution is non-uniform along the flow path owing to the horizontal cross flow [24]. The main cause for the horizontal cross flow is that the waste fluid cannot be discharged from the heat sink in time. In addition, compared with microchannel cooling, the inadequacy of cooling area prevents the strength of high-speed jets from being fully utilized [26].

To further enhance the heat removal capacity, some scholars have started to design novel heat sink structures to utilize the strengths of both cooling methods. Mudawar was one of the pioneers to study the hybrid jet impingement/microchannel heat sink (JIMHS) [24,34,35]. By adopting experiment and numerical simulation, they investigated the single-phase and two-phase heat removal capacity of JIMHS with different jet patterns and jet hole shapes. To better compare the difference in heat removal capacity and flow resistance characteristics of different cooling technologies, Deng et al. experimentally evaluated the comprehensive performance of three cooling technologies, i.e. microchannel cooling, jet impingement cooling and hybrid jet impingement/microchannel cooling [36]. The results show that the heat dissipation capacity of JIMHS is much higher than that of utilization of single cooling technology. To further enhance the heat removal capacity of JIMHS, some researchers have attempted to insert different disturbing structures into microchannels, such as pillars [37], dimples [38] or fins [39]. In addition to extending the cooling area, the disturbing structures can enhance the heat removal capacity via flow mixing and boundary layer interruptions.

Although the hybrid schemes proposed in the above studies utilizes the advantages of both cooling technologies, the lack of the waste fluid discharge design allows the presence of horizontal cross flow adverse effects. To solve this problem, Peng et al. [40] proposed a multi-jet impingement/microchannel heat sink with distributed outlet jets and numerically investigated its heat transfer and flow resistance characteristics. The results show that the heat sink with distributed outlet jets achieves lower thermal resistance, less pumping power and higher temperature uniformity than conventional microchannel heat sink. Apart from the numerical research, Gonzalez-Valle et al. [41] fabricated the jet impingement/microchannel heat sink with inlet/outlet manifolds using 3D printing and investigated the effects of the number of jets, chamber depth and the inclusion of area enhancement features on the heat transfer performance. The results show that an increase in the number of jets results in a slightly larger pressure drop and the heat sink with 16 jets exhibits the best hydraulic performance. Additionally, Wei et al. [42] investigated the multi-jet impingement heat sink with distributed returns using a programmable thermal test chip. The results demonstrate that the heat sinks with distributed returns realizes better heat transfer performance than that with common outlet since the horizontal cross flow effect could be largely reduced. After that, they further investigated the effects of jet array parameters design, i.e. nozzle density, cavity height and nozzle diameter, on thermal-hydraulic performance of the heat sink [43]. More relevant studies on heat sink with waste fluid discharge structures can be found in Refs [44,45]. Although the above novel heat sink designs achieves the timely discharge of the waste fluid, its structures are usually complex and can only be manufactured by 3D printing, resulting in higher processing costs and material selectivity. Additionally, in previous numerical studies on optimizing structural parameters of the JIMHS, professional

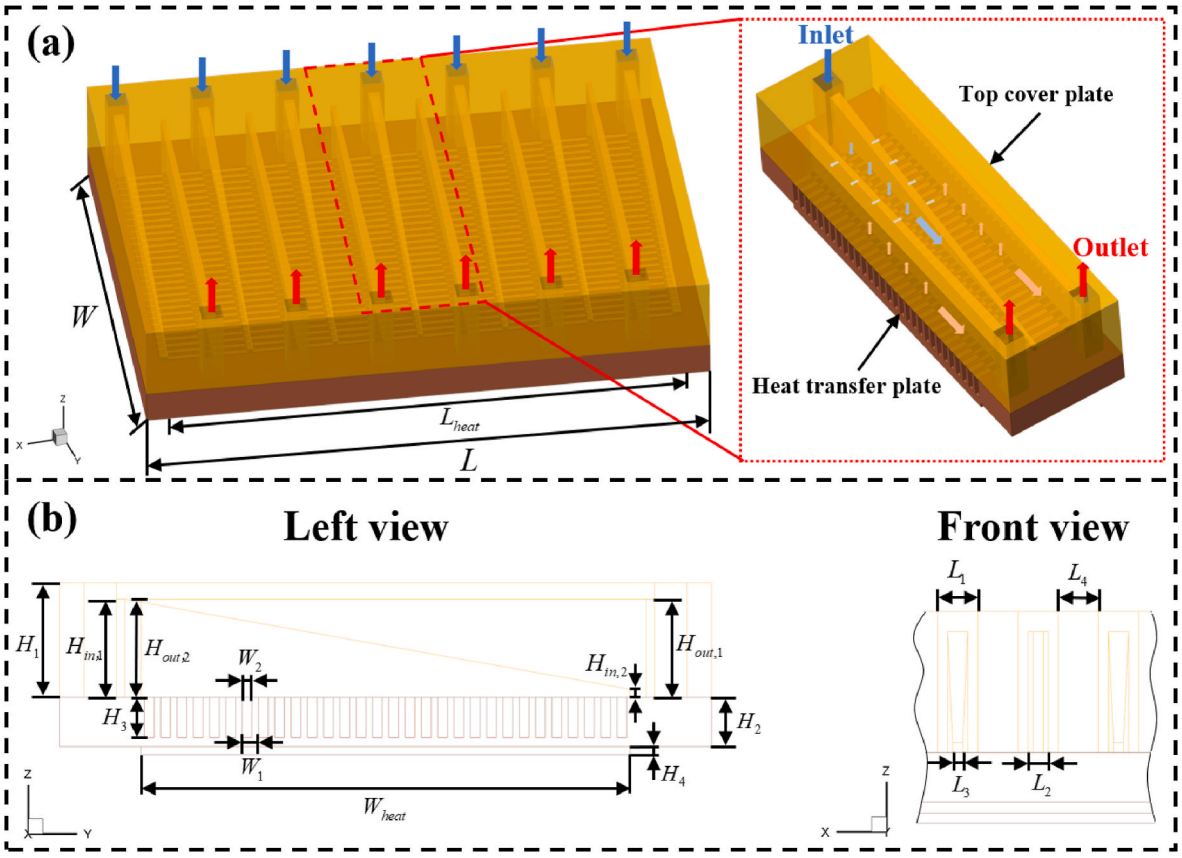

Fig. 1. (a) The three-dimensional model of the optimal SJIMHS; (b) Different views and detailed dimensions of the optimal SJIMHS.

Table 1
Structural parameters of the optimal SJIMHS (Units: mm, except for φ).

L	W	L_{heat}	W_{heat}	L_1	L_2
53	40	49	30	2	1
L_3	L_4	W_1	$\varphi = \frac{W_2}{W_1}$	H_1	H_2
0.5	2	1.03	0.58	7	3
H_3	H_4	$H_{in,1}$	$H_{in,2}$	$H_{out,1}$	$H_{out,2}$
2.44	0.5	6	0.5	6	6

optimization algorithms were rarely used, and many studies were limited to parametric analysis.

In previous research [46], the authors have proposed a hybrid slot jet impingement/microchannel heat sink (SJIMHS), which integrates the strengths of slot jet impingement and microchannel cooling, and extracts the waste fluid in time. Compared with the complex structures investigated in the literature, the SJIMHS adopted in this work has a simple structure and is easy to manufacture by conventional machining process. By performing overall 3D modeling and numerical simulations of the SJIMHS, the impact of structural parameters, i.e. channel unit width, channel height, channel width ratio and inlet/outlet branch passage inclination, on cooling capacity and flow resistance behaviours have been evaluated. Afterwards, the multi-objective optimization of some key structural parameters is performed using a combination of artificial neural network (ANN) training and genetic algorithm to derive the optimal compromise solution. In this work, to assess the practical cooling capacity and flow behaviours of the optimal SJIMHS, the corresponding heat sink is machined and tested experimentally. By varying test conditions, the impact of heat flux, inlet mass flow rate and inlet temperature variations on the cooling and flow behaviours of the optimal heat sink were investigated. In addition, a 3D numerical calculation was also performed for the optimal heat sink, and the simulation and experimental results are compared.

2. Numerical calculation model and methodology

2.1. Geometric model

Fig. 1(a) portrays the 3D geometric model of SJIMHS, which is selected from the Pareto front as the optimal compromise solution. The different views and detailed sizes of the hybrid heat sink are illustrated in Fig. 1(b) and Table 1. The hybrid heat sink includes two parts, the top cover plate and the heat transfer plate. The inlet and outlet branch passages are processed on the top cover plate for the uniform distribution of the coolant and timely evacuation of the spent fluid, as depicted in Fig. 1(a). The microchannel channels are processed on the heat transfer plate and combined with the top cover plate to form the fluid cooling pathway. The constant heating power is added on the bottom of the heat transfer plate. Generally, the cooling medium enters the heat sink from the inlet and later is distributed through the inlet branch passages. To ensure even distribution of the coolant, the inlet branch passages are processed to a tapered shape. The coolant from the inlet branch passage will vertically impinge the bottom surface of the microchannel and later flow along the microchannel after a 90° turn. Afterwards, the fluid in the microchannel converges in the outlet branch passages after a 90° turn and eventually exits the heat sink through the outlet. Different from the inlet branch passages, the outlet branch passages are not tapered, i.e. $H_{out,1} = H_{out,2}$. The major reason for the structure disparity between the inlet branch passage and outlet branch passage is the different influence of their inclination ratio on the uniformity of coolant distribution. More detailed information can refer to the authors' optimization research [46].

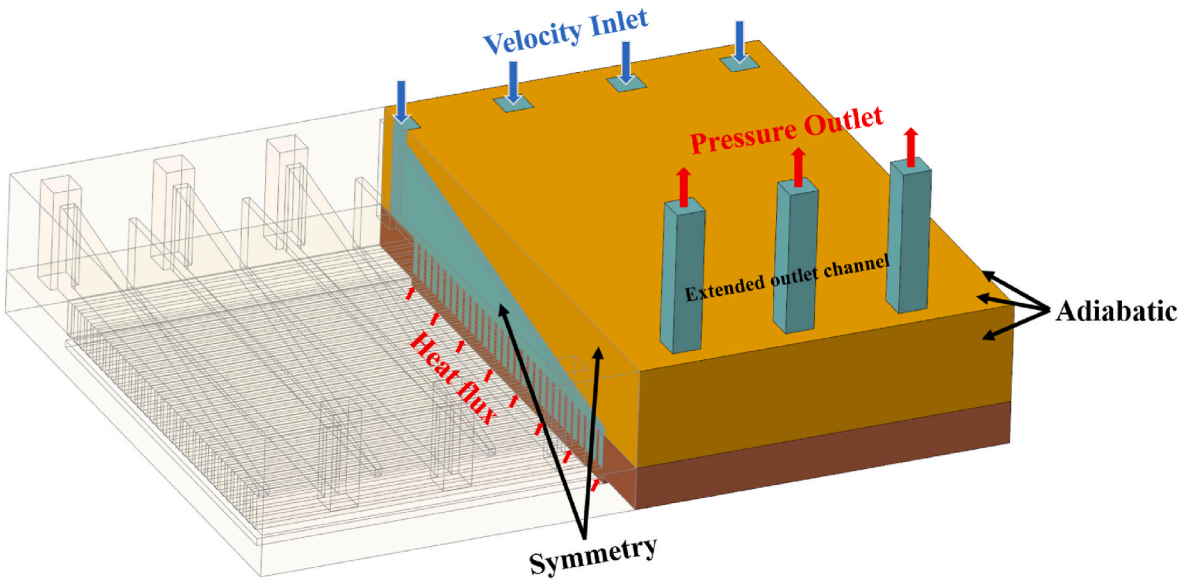

Fig. 2. The 3D computation model and boundary conditions.

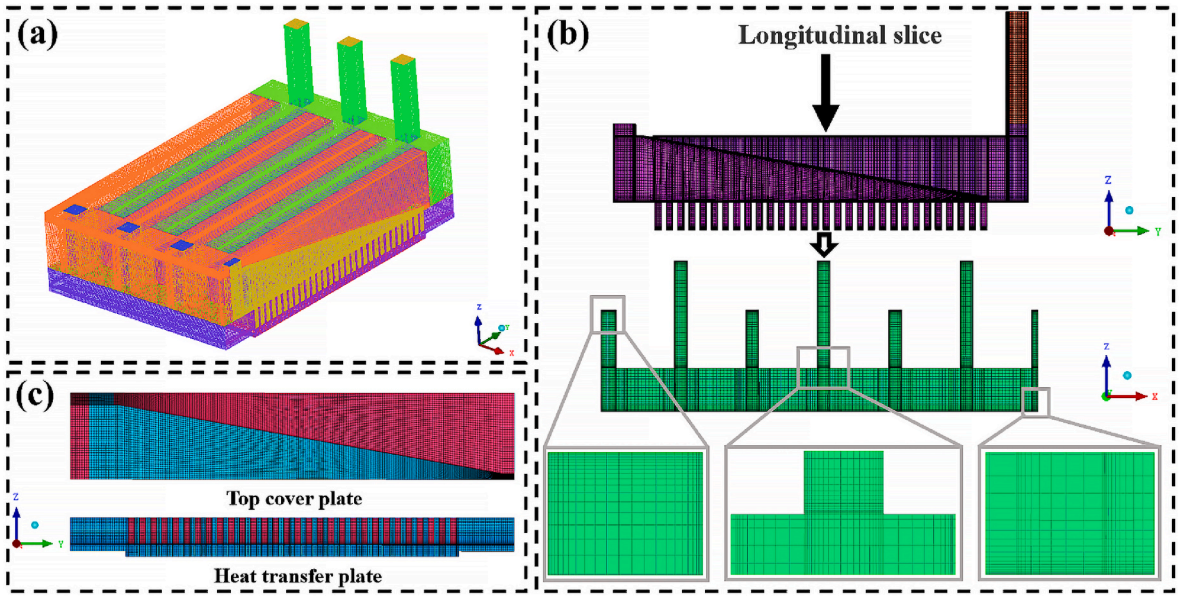

Fig. 3. (a) The entire meshing of the optimal heat sink; (b) The mesh refinement information of the fluid region; (c) The mesh of the solid region.

2.2. Governing equations and calculation settings

On the basis of previous turbulence model validation results [46], the Realizable k-ε model with higher prediction accuracy is used for numerical simulation in this research. The calculations are executed by using the solver of the software Fluent 16.0. Additionally, to simplify the numerical simulation, the flow inside the heat sink is supposed to be continuous, incompressible and steady-state. The governing equations and the calculation setups refer to the authors' previous research [46].

2.3. Boundary conditions and meshing strategy

Fig. 2 depicts the 3D calculated model and boundary conditions for the numerical calculations. As the whole heat sink model is symmetrical on the x-axis, one half of the entire model is selected as the calculated model. To avoid the influence of outlet backflow on the calculational results, the outlet was extended to 5 times the outlet hydraulic diameter in the calculation. As depicted in the figure, the velocity inlet and pressure outlet are used for the heat sink inlet and outlet, respectively. The inlet velocities of 1 m/s, 1.5 m/s, 2 m/s, 2.5 m/s, 3 m/s and 3.5 m/s are studied, and the inlet temperature for each velocity condition are 283 K, 288 K and 293 K. As for thermal conditions, a uniform heat flow density is added on the bottom of the heat transfer plate, which has a footprint of 49 × 30 mm^2. The investigated heat flow densities range from 40 W/cm^2 to 200 W/cm^2 with an increasement of 20 W/cm^2. The interface-coupled thermal condition is used for the liquid-solid interface. The adiabatic boundary conditions are used for the outer surfaces, except for the symmetry plane and heated surface.

Fig. 3 presents the entire mesh and local mesh refinement info of the computation model. To facilitate the hexahedral meshing, each part of the heat sink is meshed separately. Afterwards, the meshes of each part are merged into the entire mesh by using the software ICEM 16.0. Additionally, to meet the requirements of the enhanced wall treatment function, i.e. $y^+ \approx 1$, the height of the first layer on the solid-liquid contact

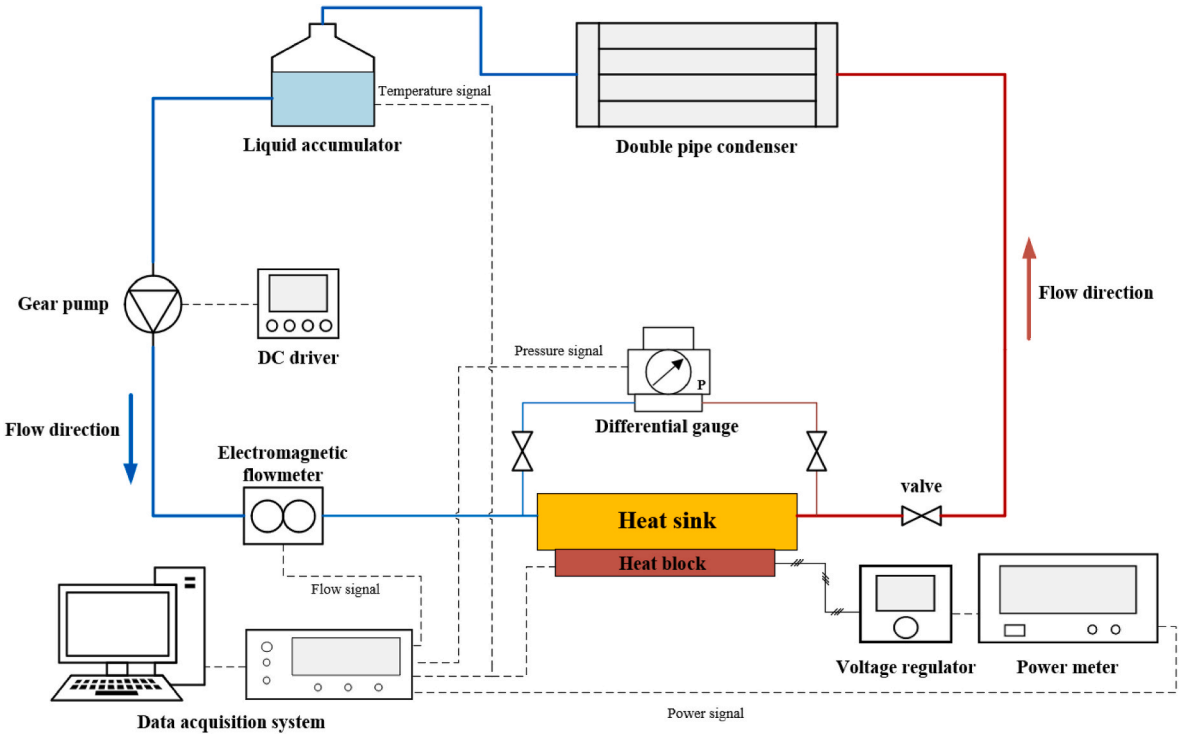

Fig. 4. Schematic diagram of the experiment testing system.

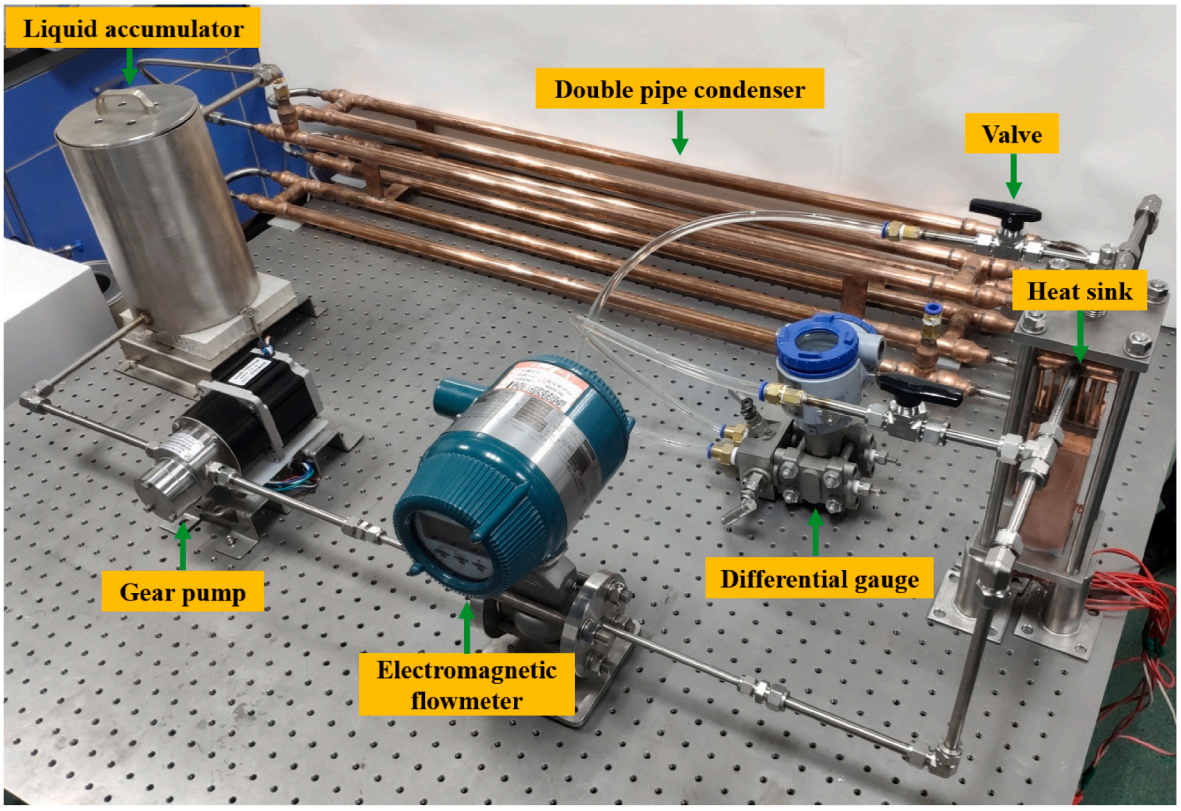

Fig. 5. Photo of the experiment testing system.

surface is set as 0.01 mm, and the growth ratio is set as 1.2. The mesh refined strategy for the fluid domain is the same as the previous simulations and more information on mesh refinement and grid independence verification can be found in the previous work [46].

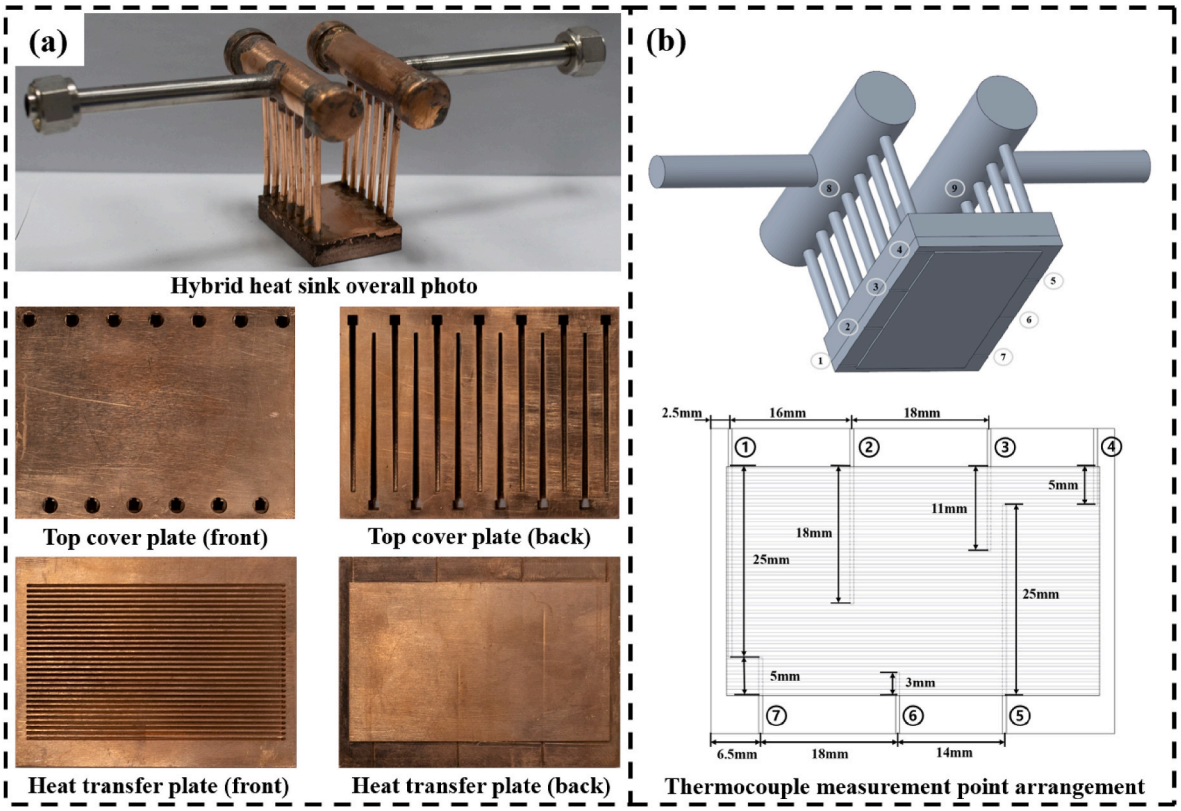

Fig. 6. (a) Photo of test heat sink; (b) Thermocouple measurement points distribution.

3. Experimental test methods

3.1. Experiment system

Fig. 4 depicts the schematic diagram of the experiment testing system built in this work with water as the cooling medium. The experiment system consists of two main segments, i.e. the system components and the control and measurement components. As show in Figs. 4 and 5, the system components of the experiment testing system are the hybrid heat sink, heat source, double pipe condenser, liquid accumulator and gear pump. The control and measurement components are the DC driver, electromagnetic flowmeter, differential gauge, thermocouple, voltage regulator and power meter. Additionally, all the measurement information is finally collected through the data acquisition system. Fig. 5 presents the photo of the experimental testing system containing the main components.

3.2. The main system components

3.2.1. Hybrid slot jet impingement/microchannel heat sink

Fig. 6(a) presents the photograph of each part and the photograph of the heat sink after welding. Each part of the heat sink is made of copper and processed using machine cutting and electrical etching techniques. After machining, each part is cleaned with acetone and alcohol, then assembled and welded using argon-arc welding and silver solder. The heat sink after welding is pickled and passivated by using the acid-washing-passive solution. To capture the temperature information of the heated surface, a total of seven thermocouple holes with a diameter of 0.5 mm are processed at both ends of the heat sink. The thermocouple holes are 0.5 mm above the heated surface, and the location and distribution information of thermocouple holes are presented in Fig. 6(b). Additionally, to acquire the inlet and outlet temperature of the coolant, two temperature measurement points are arranged at the inlet and

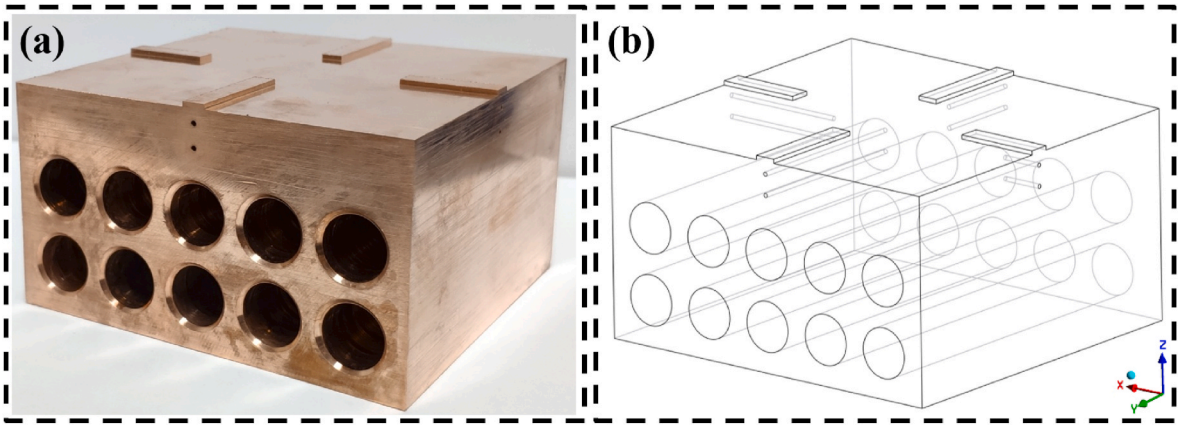

Fig. 7. Photo and 3D perspective view of heat source.

Table 2
Specification parameters of control and measurement components.

Component name	Model number and parameters
Gear pump	Model number: MG415XK/DC48W-400
Electromagnetic flowmeter	Model number: AXF005G, Range: 0–6 L/min, accuracy class: ±0.35 %
Differential gauge	Model number: FKCT35V5, Range: 0–100 kPa, accuracy class: ±0.065 %
Data collector	Model number: Keithley-2700
Voltage regulator	Model number: TDGC2
Power meter	Model number: PF9800, accuracy class: 0.5
Thermocouple	Model number: WRNK-191, accuracy class: ±0.4 K
DC driver	Model number: MP6010D

outlet dispensers, such as measurement points No.8 and No.9 in Fig. 6 (b).

3.2.2. Heat source

As presented in Fig. 7, a copper block is adopted as the simulated heat source, which is processed by machine cutting. A total of ten blind holes with a diameter of 12 mm are processed on the one side of the heat source for inserting the heating rods. Each heating rods can provide a maximum power of 300 W. To facilitate the positioning with the heated surface of the heat sink, four positioning rectangular blocks are machined on the top of the heat source. To diminish the contact thermal resistance, the heat source and heat sink are fixed with screws after applying a thin layer of thermal conductive grease on the contact surface. In order to monitor the heat source temperature and to avoid the temperature exceeding the tolerance temperature of the heating rods, a total of eight thermocouple holes with a diameter of 1 mm are machined around heat source for inserting thermocouples. The uppermost thermocouple holes are 3 mm from the top surface, and the distance between the top and bottom thermocouple holes is 5 mm.

3.3. Introduction of control and measurement components

The main control and measurement components have been described in section 3.1, and the relevant specification parameters are displayed in Table 2.

3.4. Experimental test conditions

In this work, the impact of varying inlet temperature, heating power and volumetric flow rate on the cooling capacity and flow resistance behaviours of the optimal heat sink has been investigated. Three different inlet temperatures, i.e. 283 K, 288 K and 293 K, are studied in the experiment. Six different volumetric flow rates are measured at each inlet temperature, where the inlet volumetric flow rates are 1.68 L/min, 2.52 L/min, 3.36 L/min, 4.2 L/min, 5.04 L/min and 5.88 L/min. The determination of the inlet volumetric flow rate is based on previous numerical simulation conditions. Additionally, at each inlet volumetric flow rate, nine different heat fluxes are experimentally investigated, starting from the minimum of 40 W/cm^2 to the maximum of 200 W/cm^2 with an increasement of 20 W/cm^2.

3.5. Heat source temperature prediction and heat leakage analysis

Since the maximum heat flux can reach up to 200 W/cm^2, the total heating power of the heat source is about 2940 W. With such a high heat flux, an unreasonable heat source structure may lead to the temperature of the heating rods exceeding the safety temperature, i.e. 623 K. Additionally, when the heat source insulation measures are not reasonable, it may cause heat leakage. Therefore, to prevent the occurrence of the above situations, the heat source is designed to avoid the sudden changes in area, which may lead to a large temperature gradient. In addition, to prevent the large thermal resistance due to long copper block, the heating rods are inserted laterally instead of from the bottom side. As illustrated in Fig. 8, to effectively reduce heat leakage, the heat sink is wrapped with 2 mm thick aluminosilicate fiber after the insertion of the heating rod. The aluminosilicate fiber can withstand high temperatures of around 1273 K with a thermal conductivity of only 0.035 W/(m·K). The heat source wrapped with aluminosilicate fiber is fixed on the base made of PEEK, a high temperature resistant material with a thermal conductivity of 0.04 W/(m·K). After that, a 10 mm thick rubber insulation cotton is adopted to wrap the heat source again to reduce heat leakage losses further. The thermal conductivity of the rubber insulation cotton is only 0.04 W/(m·K).

To validate the efficacy of the aforementioned insulation design, numerical simulation was undertaken utilizing the software Fluent 16.0 to estimate the heat leakage and explore the maximum temperature of the heat source. Since the problem is a simple thermal conductivity problem, the simulation is accurate enough for pure solids with residuals of 10^{-12} for the energy equation. The boundary conditions are presented in Fig. 8 h_{hs} is corresponding to the average convective heat transfer coefficient of the heat sink, and h_{nc1} and h_{nc2} are equivalent to the

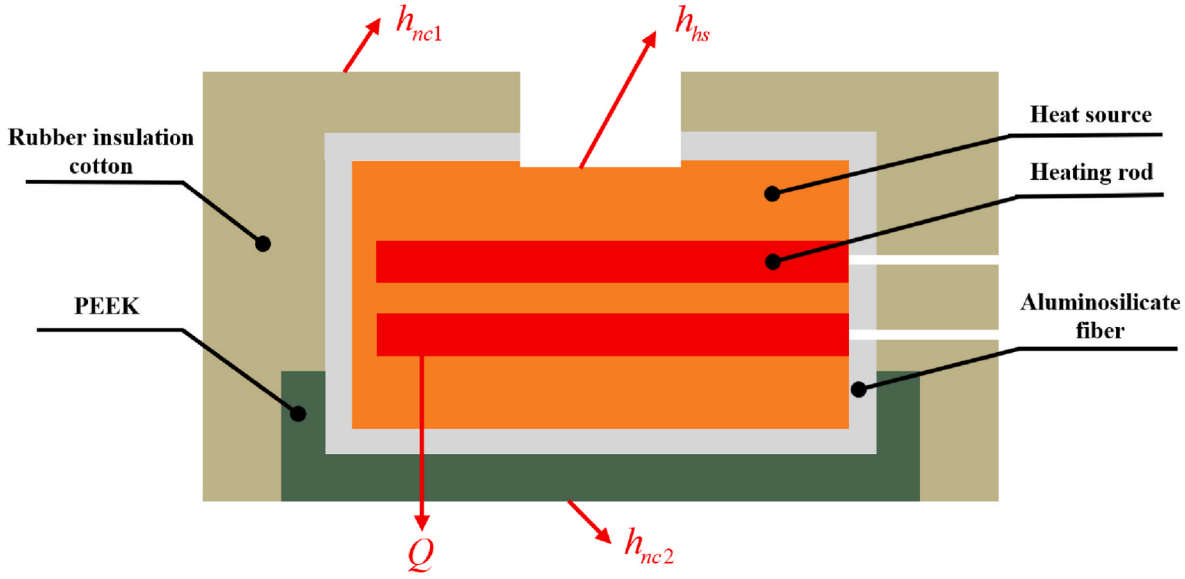

Fig. 8. Schematic diagram of heat source simulation and boundary conditions.

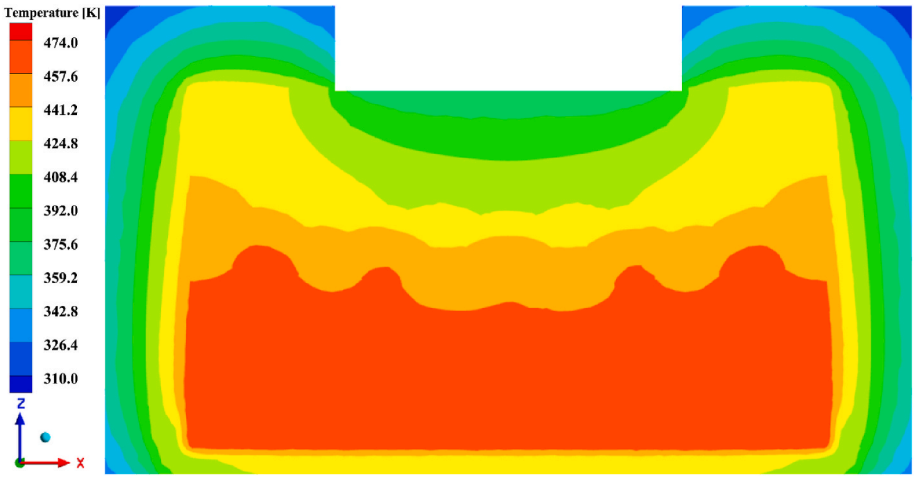

Fig. 9. Temperature distribution of z-x cross section of heat source.

natural convective heat transfer coefficient of the PEEK base and insulation cotton surface. The internal heat source term Q is used to represents the heating power of the heating rods. The main material of the heating rod is MgO, whose thermal conductivity is taken as 36 W/(m·K). The heating power is set to 2940W, which corresponds to the maximum heat flux of 200 W/cm^2 on the heated surface. Based on the numerical simulation results before, the equivalent convective heat transfer coefficient, i.e. h_{hs}, is taken as 6 W/(cm^2·K), corresponding to the lowest inlet volumetric flow rate. Since the heated surface of the heat sink is tightly pressed against the heat source, the free stream temperature is set to be the average temperature of the heated surface, i.e. 353 K. The equivalent natural convective heat transfer coefficient, i.e. h_{nc1} and h_{nc2}, is taken as 5 W/(m^2·K) and the ambient temperature is set to 298 K, which is a reasonable value for natural convection.

Fig. 9 shows the temperature distribution of the z-x cross section of the heat source obtained from the simulation. Clearly, the maximum temperature is about 474 K, which is much lower than the maximum temperature of 623 K that the heating rod can withstand. Additionally, the temperature around the insulation material is low, which indicates that the use of double-layer insulation design can achieve a good insulation. By integrating the heat flow density at the contact surface of the heat source, it could be calculated the heat taken away by heat sink is 2873 W. Therefore, the heat dissipated to the environment is only 67 W and the percentage of heat leakage is only 2.3 %, which further validate the insulation design is effective. Moreover, the above simulated working condition is the worst case of heat source cooling, i.e. the most serious case of heat leakage, and the heat leakage loss will be less than 2.3 % in other conditions. In the experimental test, the heat source and PEEK base are fixed to the bracket and then the bottom surface of the PEEK is also wrapped with rubber insulation cotton.

3.6. Data reduction and uncertainty analysis

Considering the distance of the thermocouples from the heated surface and heat transfer surface, the average temperature of the heated surface ($\overline{\overline{T}}_{heat}$) and heat transfer surface ($\overline{\overline{T}}_{trans}$) could be calculated by following equations:

$$\overline{T}_{heat} = \frac{1}{7}\sum_{i=1}^{7} T_i + \frac{Q\Delta z_1}{A\lambda_s} \tag{1}$$

$$\overline{T}_{trans} = \frac{1}{7}\sum_{i=1}^{7} T_i - \frac{Q\Delta z_2}{A\lambda_s} \tag{2}$$

where $T_1 \sim T_7$ is the temperature measured by thermocouples, Q is the heating power of the heating rods, A is the heated surface area, i.e. 49 × 30 mm^2, Δz_1 is the distance from the thermocouple holes to heated surface, i.e. 0.5 mm, and Δz_2 is the distance from the thermocouple holes

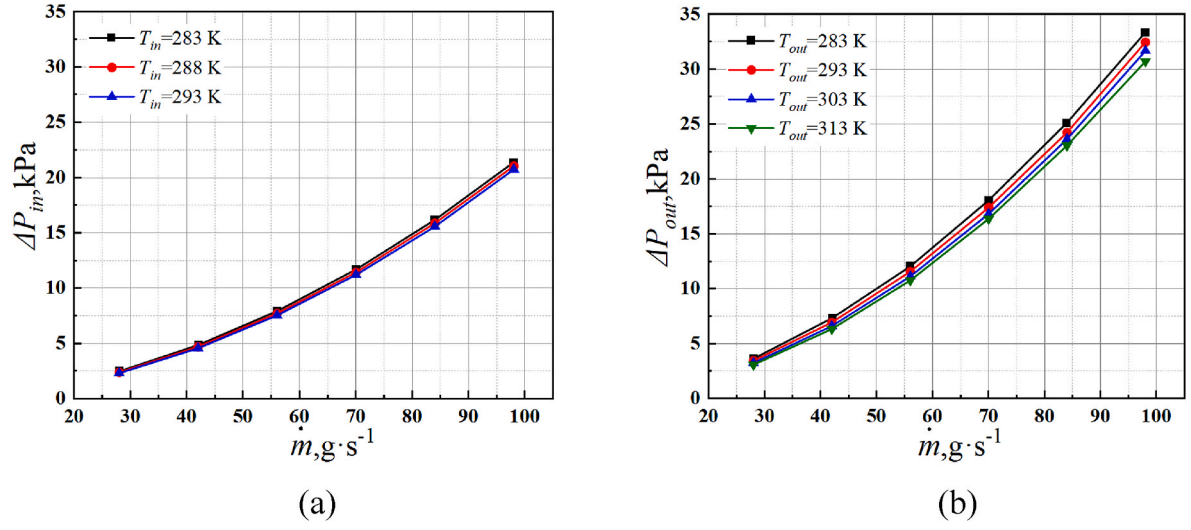

Fig. 10. (a) Pressure loss in inlet liquid-distributor and (b) pressure loss in outlet liquid-distributor under different working conditions.

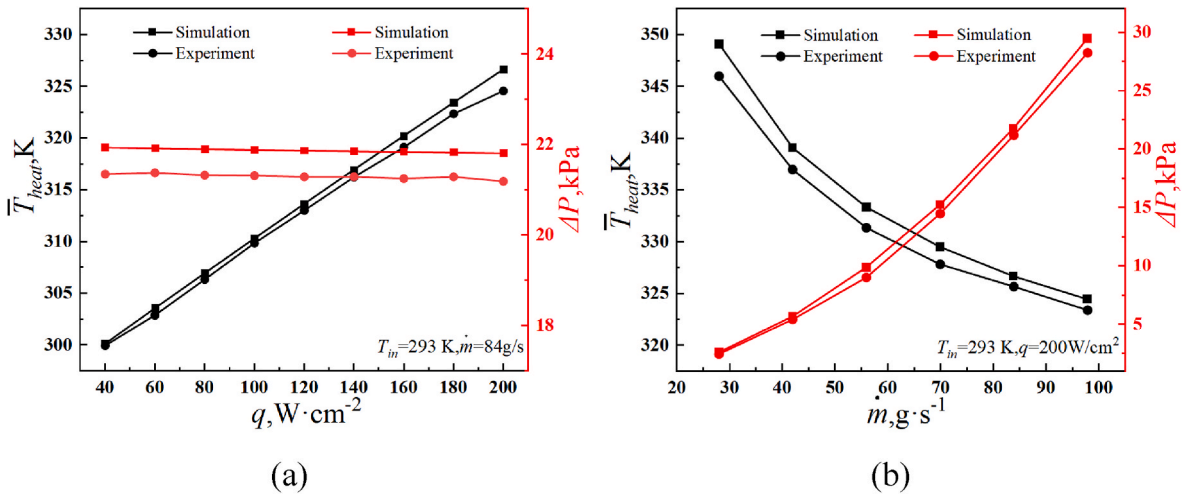

Fig. 11. (a) Comparison of experimental and simulation results at different heat fluxes; (b) Comparison of experimental and simulation results at different inlet mass flow rates.

to the center of gravity position of the microchannel, i.e. 1.78 mm.

The average convective heat transfer coefficient ($\overline{\overline{h}}$) is defined as below:

$$\overline{h} = \frac{Q}{A\left(\overline{T}_{trans} - T_f\right)} \tag{3}$$

where T_f is the average temperature of the heat sink inlet and outlet.

To assess the uniformity of the heated surface, the difference between the temperature measurement values obtained by each thermocouple and the average value is made, defined as below:

$$\Delta T_{ave,j} = T_j - \sum_{i=1}^{7} T_i \tag{4}$$

where j takes values from 1 to 7, representing the thermocouple number.

Since the pressure drop obtained from the differential gauge in the experiment includes the pressure loss inside the inlet and outlet liquid-distributors, the pressure drop of the heat sink is defined as:

$$\Delta P = \Delta P_{test} - \Delta P_{in} - \Delta P_{out} \tag{5}$$

where ΔP_{test} is the pressure drop recorded with a differential gauge, ΔP_{in}

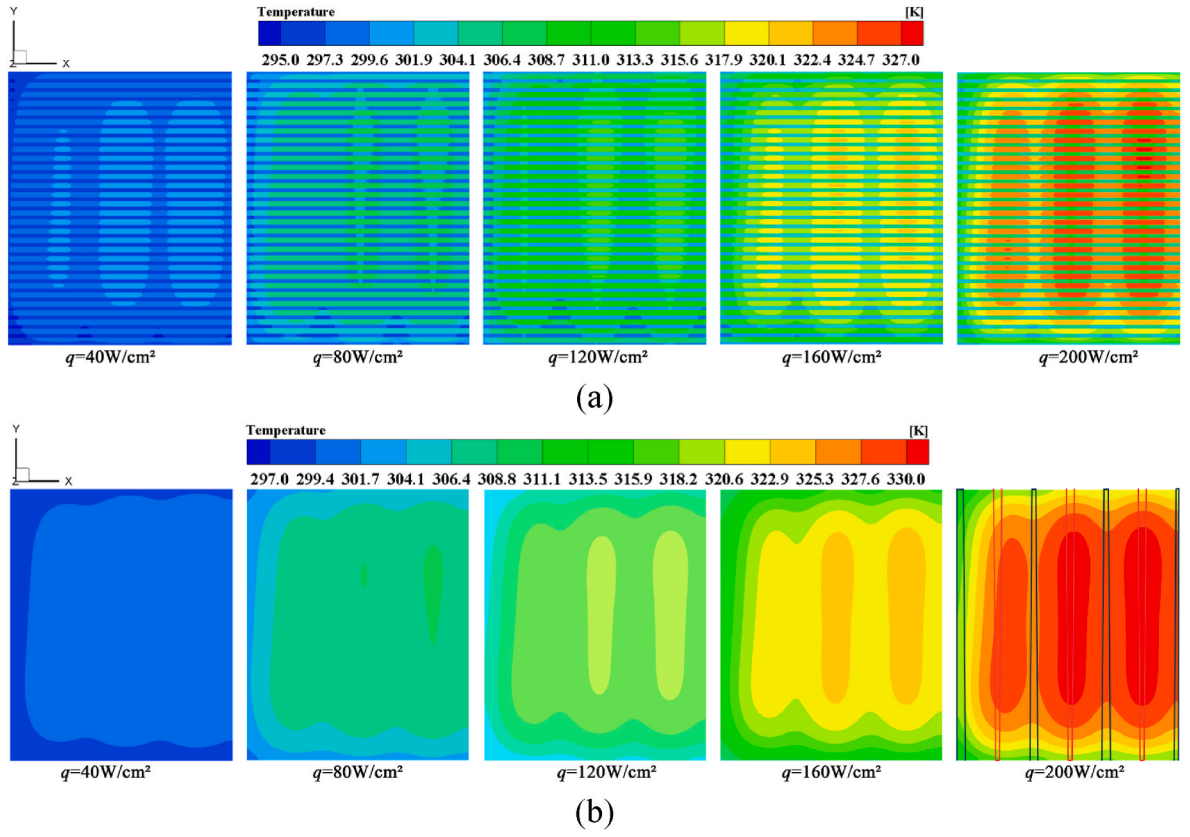

Fig. 12. Temperature contours of (a) heat transfer surface and (b) heated surface under different heat fluxes (V_{in} = 3 m/s, T_{in} = 293 K, $\dot{m}$ = 84 g/s).

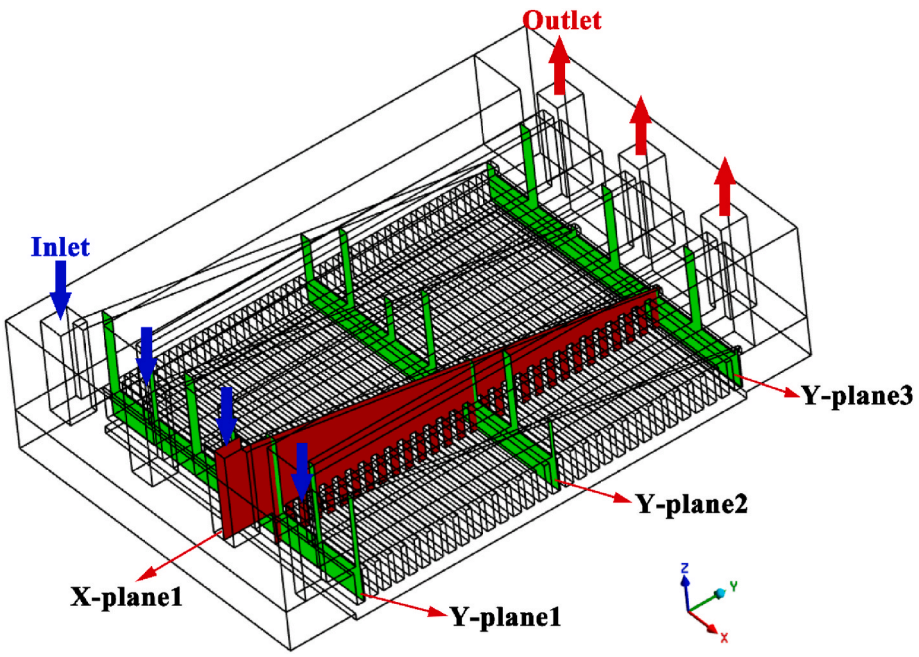

Fig. 13. The relative position of different cross sections in heat sink.

and ΔP_{out} are the pressure loss of the inlet and outlet liquid-distributors, respectively. Considering that the error in estimating the pressure loss of the liquid-distributor may be large by using the empirical correlation, the inlet and outlet liquid-distributor are modeled and simulated separately to obtain the pressure loss under varying operating conditions. The turbulence model and calculation settings are the same as the calculation of the heat sink. Fig. 10 presents the pressure loss of inlet and outlet liquid-distributors under various working conditions. When the outlet temperature is in the middle of the four calculated temperatures, the corresponding pressure drop of outlet liquid-distributor is obtained by the linear difference of the adjacent calculated points.

The heat sink's pumping power is defined as below:

$$W_{pumping} = \Delta P \dot{V} \tag{6}$$

where $\dot{V}$ is the inlet volume flow rate.

The absolute error and accuracy class of the measurement components have been given, as illustrated in Table 2. Therefore, the uncertainty of $\overline{\overline{h}}$ due to the accuracy of the thermocouples and power meter is within ±1.1–10.1 % based on the following calculation equations [47]:

$$\frac{\delta \overline{\overline{h}}}{\overline{\overline{h}}} = \sqrt{\left(\frac{\delta Q}{Q}\right)^2 + \left(\frac{\delta y_1}{y_1}\right)^2} \tag{7}$$

$$\delta y_1 = \sqrt{\sum_{i=1}^{7}\left(\frac{1}{7}\delta T_i\right)^2 + \left(\frac{\Delta z_2}{A\lambda_s}\delta Q\right)^2 + \left(\frac{1}{2}\delta T_{in}\right)^2 + \left(\frac{1}{2}\delta T_{out}\right)^2} \tag{8}$$

$$y_1 = \frac{1}{7}\sum_{i=1}^{7} T_i - \frac{Q\Delta z_2}{A\lambda_s} - \frac{1}{2}(T_{in} + T_{out}) \tag{9}$$

4. Results and discussions

4.1. Comparison of numerical simulation results with experimental results

Fig. 11 presents the comparison between the numerical simulation results and experimental results under different working conditions. Observation of Fig. 11(a) reveals that $\overline{\overline{T}}_{heat}$ rises simultaneously with increasing heat flux, while ΔP remains basically the same. The change tendency of the simulation results is basically coincident with the experimental results, and the difference between them is small. Additionally, the comparison at different inlet mass flow rates indicates that $\overline{\overline{T}}_{heat}$ and ΔP change curves obtained from numerical simulation still basically coincide with those obtained from experimental measurements. In addition, comparing the relative error between the simulation results and experimental results, the maximum relative error of $\overline{\overline{T}}_{heat}$ is about 0.9 %, and the maximum relative error of ΔP is about 9.7 %. Among all the conditions compared, there is only one point where the relative error of ΔP is near 10 %, while the relative error at the other points is less than 6.5 %. Therefore, the relative errors between the numerical simulation results and experimental results are within an acceptable range. Thus, the credibility of the numerical simulation in this research can be verified.

4.2. Analysis of numerical simulation results

Fig. 12 portrays the temperature contours of the heated surface and heat transfer surface at different heat fluxes. With the increase of heat flux, the temperature of the heated surface and heat transfer surface gradually increases and the temperature distribution uniformity gradually deteriorates, reflecting in the expansion of the high temperature region. Moreover, when the heat flux is high, alternating rows of high and low temperature regions on the heated surface can be clearly observed, and the same phenomenon is also observed in Zhou's study [48]. The main reason for this phenomenon is the alternative placement of the inlet and outlet branch passages. As presented in Fig. 12(b), the corresponding locations of the inlet and outlet branch passages are marked on the figure where the heat flux is 200 W/cm^2. The black boxes represent the inlet branch passages while the red boxes represent the outlet branch passages. Noticeably, the low temperature regions are usually beneath the inlet branch passage while the high temperature regions are usually beneath the outlet branch passage. Additionally, observing the temperature distribution along the y-axis, it can be noticed that the closer to the two ends of the inlet/outlet branch passages, the lower the temperature is, and the closer to the middle core area of the inlet/outlet branch passages, the higher the temperature is.

To further analyse the causes of the difference in temperature distribution of the heated surface, the internal flow field underneath the

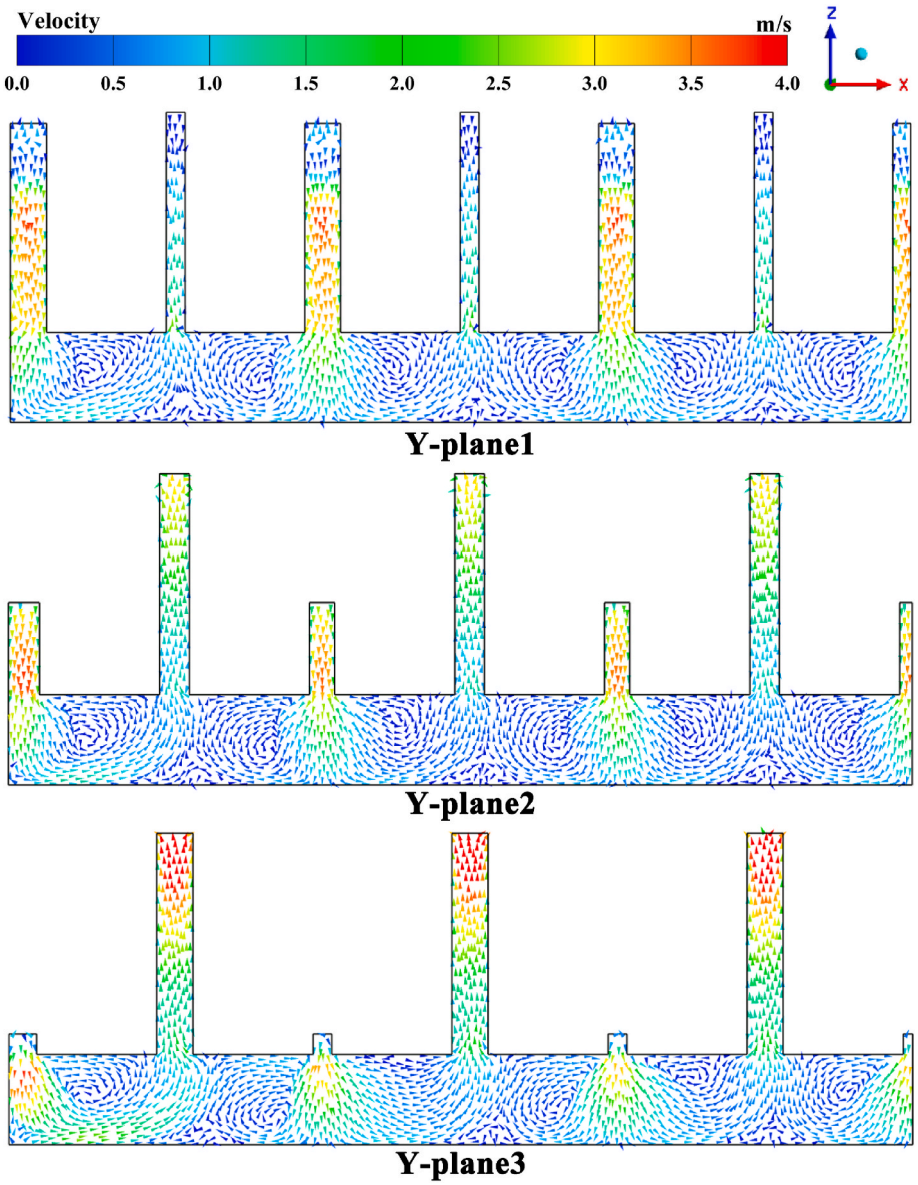

Fig. 14. Velocity vector distribution in the z-x plane of the heat sink.

inlet and outlet branch passages is analyzed. Fig. 13 presents the relative position of different cross sections inside the flow field. As shown in Fig. 14, the coolant entering the microchannel from the inlet branch passage forms an obvious jet impingement phenomenon. The coolant impinges vertically on the bottom surface of the microchannel, which enhances the heat removal capacity and thus lowers the surface temperature. In contrast, the channel surface below the outlet branch passages can only rely on fluid horizontal flushing for cooling. In addition, the diffused fluid from the jets of adjacent slot hole collides below the outlet branch passages, which will further lower the horizontal velocity of the fluid and thus weakens the cooling performance. Although the cross-sectional shape varies at different positions, the flow field structure formed within the microchannel is approximately the same. Due to the interaction of adjacent slot jets, vortex structures in clockwise and counterclockwise directions will appear at intervals within the microchannel. Additionally, the fluid temperature variation due to heat absorption along the channel flow direction is also responsible for differences in heat removal capacity.

Different from the above analysis, the reason for the difference of temperature distribution along y-axis direction is the uneven mass flow distribution of the fluid. Fig. 15 portrays the distribution of mass flow among microchannels along the y-axis direction. Obviously, the closer to the ends of the inlet/outlet branch passages, the higher the mass flow rate in the corresponding channels. Nevertheless, less fluid flows to the microchannels in the middle region. As depicted in Fig. 16(a), the velocity component along the negative z-axis is higher near the end zone, which means that more fluid will enter the corresponding channels. In addition, more fluid flows to the microchannels near the outlet than that near the heat sink inlet. The similar finding is also noticed by Zhou et al. [48,49], and there are two main reasons for this phenomenon, i.e. inlet fluid splash and uneven pressure distribution along the inlet branch passage. As depicted in Fig. 16(a), the fluid entering form the inlet impinges bottom surface of the microchannel and then splashes upward, causing a small velocity in the positive direction along the x-axis. For the microchannels close to the heat sink inlet, although affected by the splashing fluid, the velocity component in the negative direction along the z-axis is still relatively large due to inlet effect, and there is still more fluid entering the corresponding microchannels. For the microchannels in the core region, it can be seen clearly the absolute value of the velocity component in the negative direction along the z-axis is much smaller.

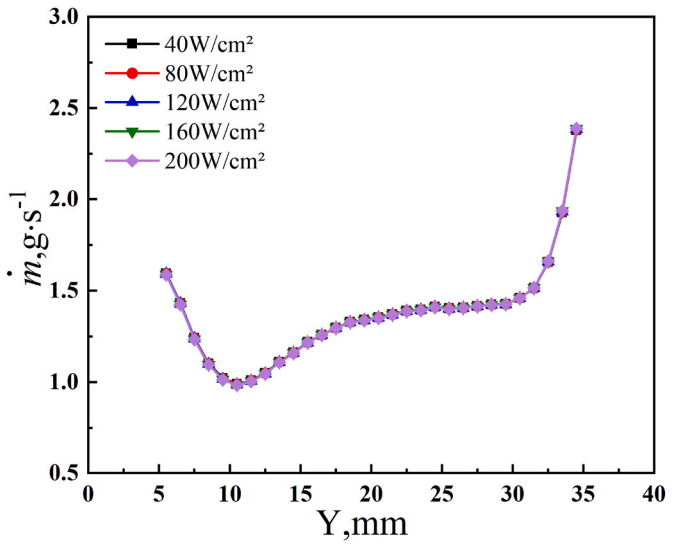

Fig. 15. The distribution of mass flow among microchannels under different heat fluxes.

The main cause is that the core region is still affected by the splashing fluid, while due to the lack of inlet effect, the velocity component in the negative direction along the z-axis is relatively small. As a result, less fluid will enter the corresponding channels due to the impact of splashing fluid. However, for the microchannels close to outlet, the fluid entering the corresponding microchannels is not impacted by the splashing fluid due to the sufficient distance from the inlet. As for the second reason, Fig. 16(b) depicts the pressure contour of the inlet branch passage. Clearly, more fluid will tend to flow into the microchannels close to the heat sink outlet as the system pressure is lowest. Although the current mass flow distribution is still uneven, it has been significantly improved compared with the pre-optimization structure, where the maximum flow rate of the microchannel is nearly 15 times higher than the minimum flow rate [46].

Fig. 17 illustrates the impact of heat flux and inlet temperature variations on heat removal capacity and flow resistance performance. With the increasing heat flux, the $\overline{\overline{T}}_{trans}$ and $\overline{\overline{T}}_{heat}$ increase linearly. Compared with the heat flux of 40 W/cm^2, the $\overline{\overline{T}}_{trans}$ rises by approximately 288 K at the heat flux of 200 W/cm^2, while the $\overline{\overline{T}}_{heat}$ rises by almost 300 K. Unlike the significant variation in temperature, the increase in heat flux has a smaller influence on ΔP and $\overline{h}$. As depicted in Fig. 17(a), the $\overline{h}$ also increases linearly and slightly with increasing heat flux. Additionally, observing Fig. 17(b), as the heat flux increases, the ΔP decreases linearly and slightly. The main cause for the subtle variations in $\overline{h}$ and ΔP is that the temperature variation affects the physical properties of the water. When the inlet mass flow rate is constant, the temperature of the coolant inside the heat sink also increases with increasing heat flux. For water, the thermal conductivity rises slightly with the increasing temperature, while the coefficient of dynamic viscosity reduces slightly as the temperature rises. As a result, the heat removal capacity and flow resistance performance of the heat sink will enhance slightly with the heat flux increasing.

Additionally, as the inlet temperature rises, the $\overline{\overline{T}}_{trans}$ and $\overline{\overline{T}}_{heat}$ also increase. The increase amplitude of $\overline{\overline{T}}_{trans}$ or $\overline{\overline{T}}_{heat}$ is essentially close to inlet temperature differences. Similar to the impact of heat flux changes on cooling capacity and flow resistance performance, the overall performance of the heat sink will improve slightly as the inlet temperature rises, and the reason is the same as above.

Fig. 18 shows the temperature contours of the heated surface and heat transfer surface at different inlet velocities. As the inlet velocity rises, the temperature of the heat transfer and heated surface gradually reduces and the temperature distribution uniformity is significantly improved. Furthermore, Fig. 19 portrays the impact of inlet velocity variations on the average temperature, average heat transfer coefficient and pressure drop. When the inlet velocity is 3.5 m/s and the heat flux is 200 W/cm^2, the maximum temperature of the heated surface is only 328 K, which is far below the commonly defined chip safety temperature

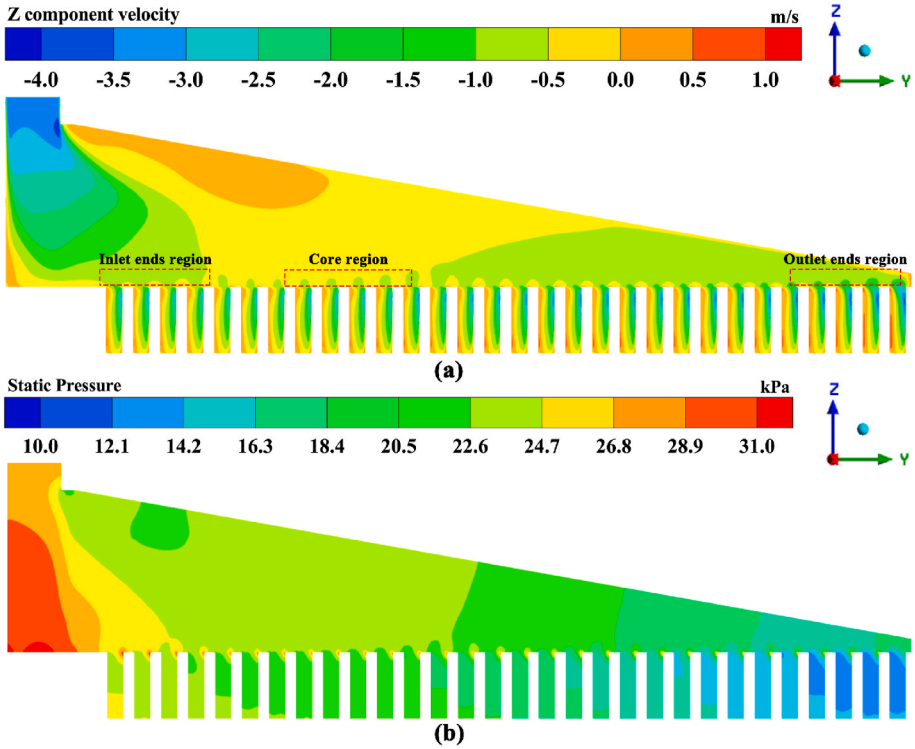

Fig. 16. The velocity and pressure contour diagram of the X-plane1: (a) Z-direction component velocity; (b) Static pressure.

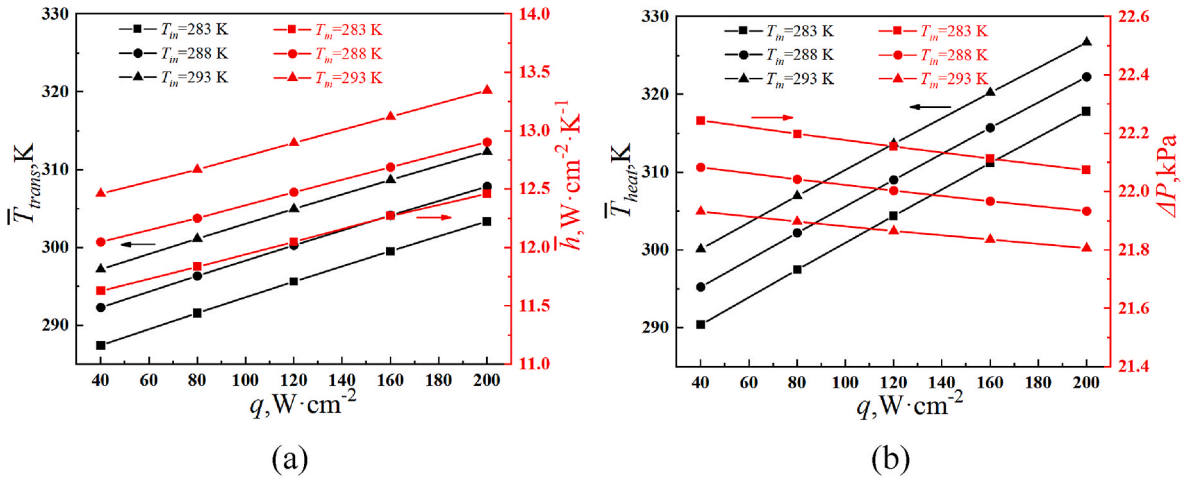

Fig. 17. (a) $\overline{\overline{T}}_{trans}$ and $\overline{h}$ under different inlet temperature and heat flux; (b) $\overline{\overline{T}}_{heat}$ and ΔP under different inlet temperatures and heat flux (V_{in} = 3 m/s, $\dot{m}$ = 84 g/s).

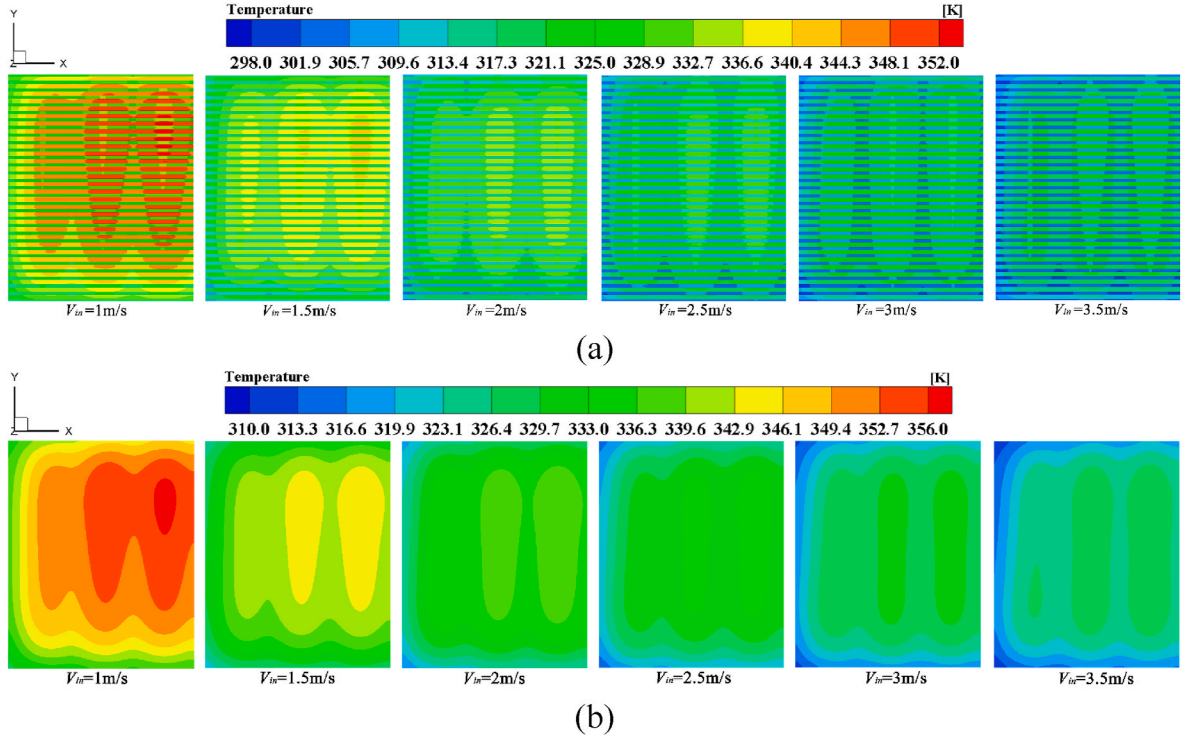

Fig. 18. Temperature contours of (a) heat transfer surface and (b) heated surface under different inlet velocity (T_{in} = 293 K, q = 200 W/cm^2).

of 358 K [50]. Although the temperature of the heated surface and heat transfer surface increases as the inlet velocity decreases, the maximum temperature of the heated surface is approximately 355 K at an inlet velocity of 1 m/s, which is still slightly below the chip safety temperature. As for the average temperature, the $\overline{\overline{T}}_{heat}$ is approximately 350 K at an inlet velocity of 1 m/s, while the pressure drop is only 2.6 kPa. In addition, observing the variation trend of the curves, it can be noticed that the downtrend of $\overline{\overline{T}}_{trans}$ and $\overline{\overline{T}}_{heat}$ is dwindled as the inlet velocity is higher than 1.5 m/s. However, the uptrend of ΔP is accelerated at the same situation. Therefore, for liquid forced cooling, it is unwise to rely on increasing the inlet mass flow rate to further improve the cooling capacity at higher inlet mass flow rates. In this situation, increasing the inlet mass flow rate provides limited improvement in cooling capacity, but will result in a significant deterioration in flow resistance performance.

4.3. Analyses of experimental results and comparison with literature results

To evaluate the practical performance of the hybrid heat sink, experimental tests were performed at various operating conditions. Fig. 20 presents the impact of mass flow rate and heat flux variations on the cooling capacity and flow resistance behaviours of the heat sink. As with the simulation results, $\overline{\overline{T}}_{trans}$ and $\overline{\overline{T}}_{heat}$ decreases as the mass flow rate rises. For the same mass flow rate, the higher the heat flux is, the higher the $\overline{\overline{T}}_{trans}$ and $\overline{\overline{T}}_{heat}$ are. When the inlet mass flow rate is minimal, the maximum difference in $\overline{\overline{T}}_{heat}$ is approximately 313 K, which corresponds to the minimum heat flux and maximum heat flux, respectively. As the inlet mass flow rate rises gradually, the difference in $\overline{\overline{T}}_{heat}$ between different heat flux decreases at the same time. Additionally, as

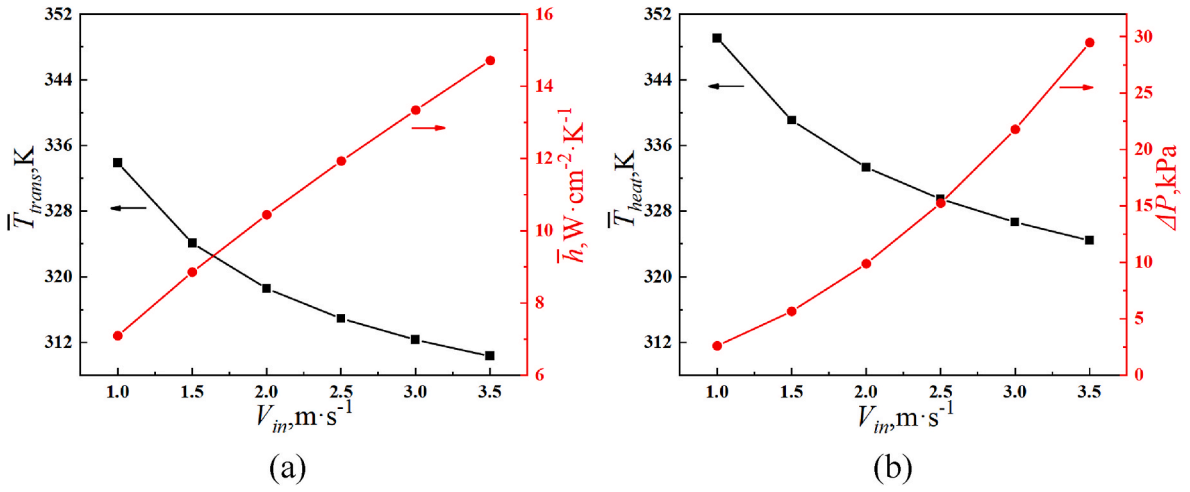

Fig. 19. (a) $\overline{\overline{T}}_{trans}$ and $\overline{h}$ under different inlet velocities; (b) $\overline{\overline{T}}_{heat}$ and ΔP under different inlet velocities (T_{in} = 293 K, q = 200 W/cm^2).

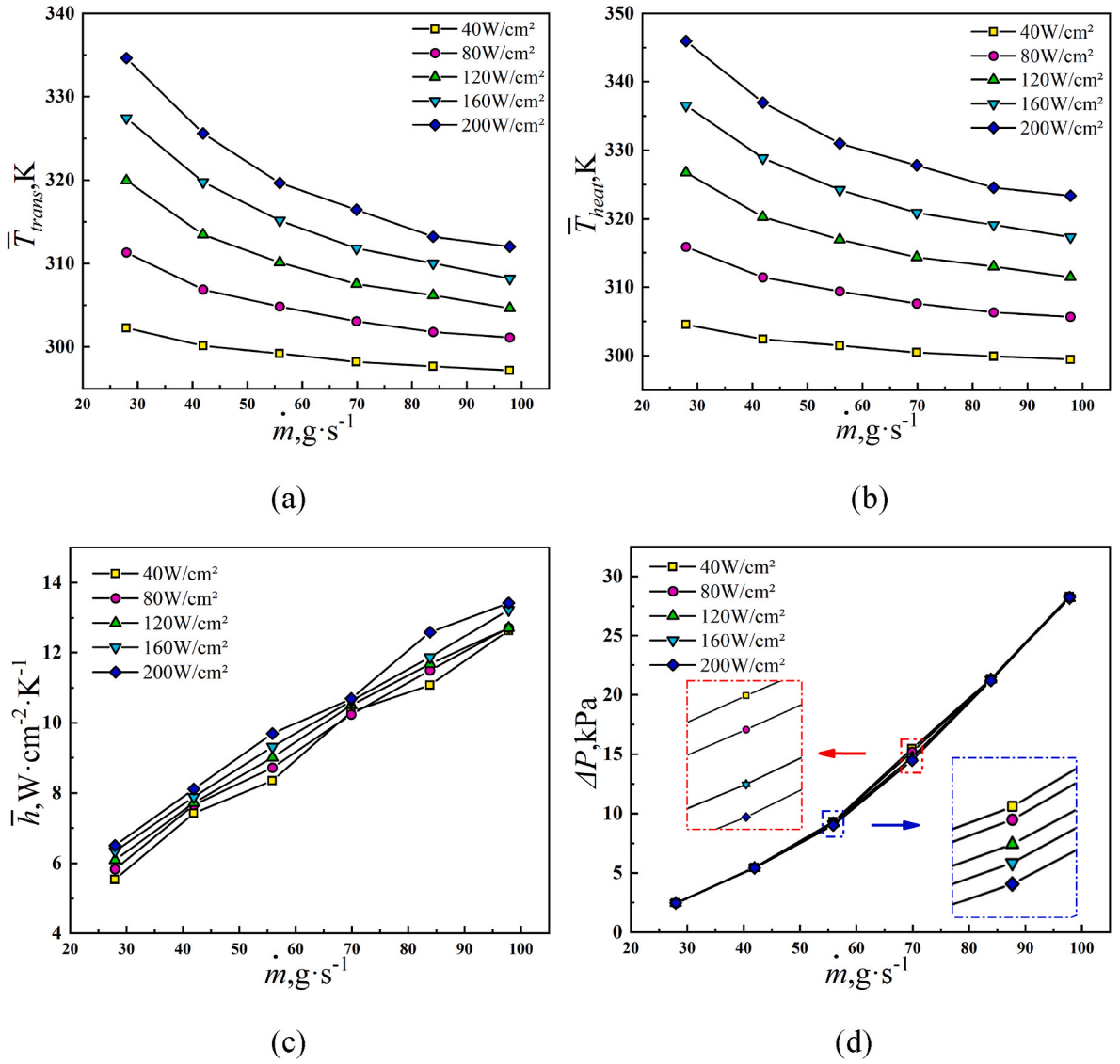

Fig. 20. (a) $\overline{\overline{T}}_{trans}$ at different mass flow rates and heat fluxes; (b) $\overline{\overline{T}}_{heat}$ at different mass flow rates and heat fluxes; (c) $\overline{h}$ at different mass flow rates and heat fluxes; (d) ΔP at different mass flow rates and heat fluxes (T_{in} = 293 K).

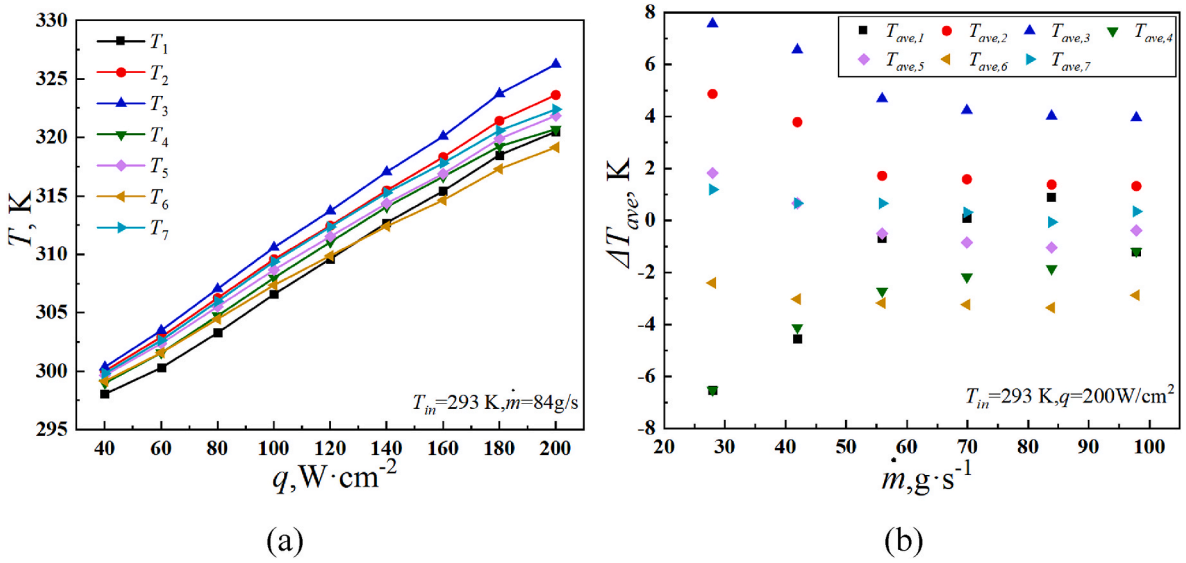

Fig. 21. (a) Comparison of thermocouple temperature measurement values at various heat fluxes; (b) Evaluation of temperature uniformity of temperature measurement point at various mass flow rate.

with the simulation results, the downtrend of $\overline{\overline{T}}_{trans}$ and $\overline{\overline{T}}_{heat}$ is dwindled as the inlet mass flow rate rises and the similar finding is also observed in the experimental research by Remco et al. [51]. The main reason is that with the increasing inlet mass flow rate, the convective heat transfer thermal resistance decreases and thus the total thermal resistance of the heat sink constantly converges to the forced water-cooling limit thermal resistance, i.e. the thermal resistance defined by the water heat capacity. In addition, as depicted in Fig. 20(c) and (d), $\overline{h}$ will slightly increase with the increasing heat flux, while ΔP will slightly reduce. This phenomenon is coincident with the simulation results, and the detailed causes have been discussed above.

As can be seen from the above numerical simulation results, high and low temperature regions alternate on the heated surface due to the alternative placement of the inlet and outlet branch passages. To demonstrate whether the same phenomenon exists in the experiment, Fig. 21(a) presents the comparison of temperature measurement values of various thermocouples under different working conditions. The location details of the thermocouples are shown in Fig. 6(b). Thermocouples 1, 2 and 4 are located below the inlet branch passages, thermocouples 5 and 7 are located below the outlet branch passages and thermocouples 3 and 6 are located below the middle position of the inlet and outlet branch passages. The subscripts in Fig. 21 represent the thermocouple numbers. Comparing the measured values of thermocouples 1, 2 and 4, it can be found that thermocouple 1 near the inlet and thermocouple 4 near the outlet have relatively lower temperature values, while thermocouple 2 in the core region has relatively higher temperature value. This is coincident with the temperature contour diagram of the heated surface in the simulation results. In addition, thermocouple 1 and thermocouple 7 are located on the same straight line, but respectively beneath the inlet and outlet branch passage. Obviously, the temperature value of thermocouple 1 is lower than the temperature value of thermocouple 7, which is also coincident with the simulation results. The main causes for this phenomenon are differences in the type of cooling mode and the coolant temperature, which have been discussed in detail previously.

To evaluate the temperature distribution uniformity of the heated surface, Fig. 21(b) presents the difference between the temperature measurement values obtained by each thermocouple and the average value. When the mass flow rate is small, the measured values of different thermocouples vary obviously, reflecting the poor uniformity of the

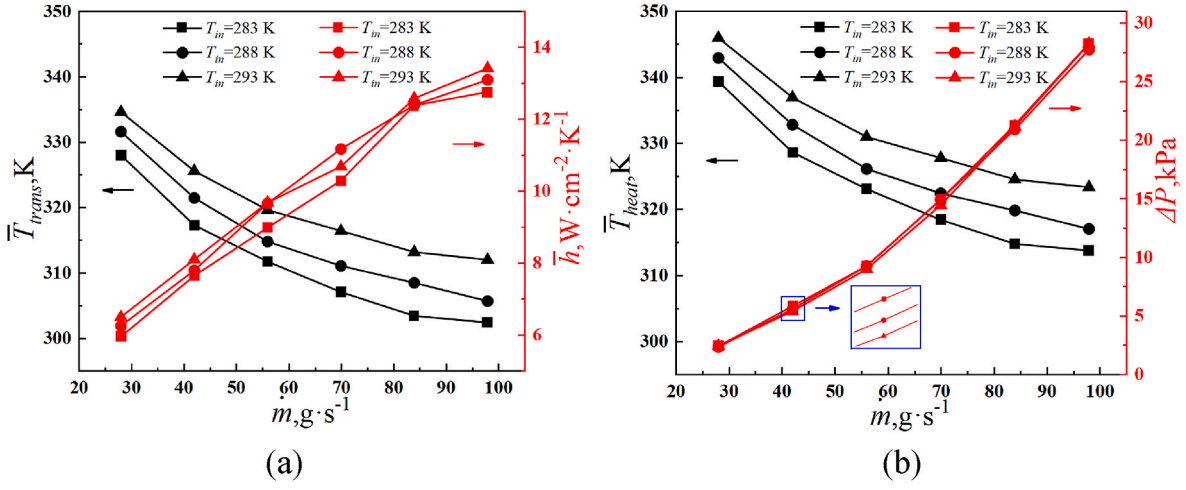

Fig. 22. (a) $\overline{\overline{T}}_{trans}$ and $\overline{h}$ at different inlet mass flow rates and inlet temperatures; (b) $\overline{\overline{T}}_{heat}$ and ΔP at different inlet mass flow rates and inlet temperatures (q = 200 W/cm^2).

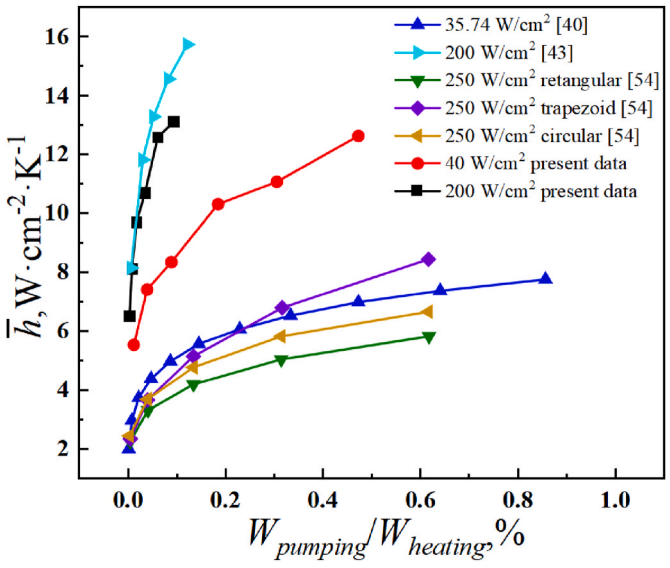

Fig. 23. Comparison of the hybrid heat sink performance between this work and previous published works.

temperature distribution. With increasing mass flow rate, the difference between the measured values of different thermocouples diminishes. When the inlet mass flow rate is 98 g/s, the maximum value of ΔT_{ave} is only 3.96 K, and the largest difference between different thermocouples is only 6.9 K.

Fig. 22 portrays the impact of inlet mass flow rate and inlet temperature variations on the cooling capacity and flow resistance behaviours of the heat sink. Similar to the numerical simulation results, the $\overline{\overline{T}}_{trans}$ and $\overline{\overline{T}}_{heat}$ rise as the inlet temperature rises, and the increase amplitude of $\overline{\overline{T}}_{trans}$ or $\overline{\overline{T}}_{heat}$ is essentially close to the difference in the inlet temperature. Additionally, with the increasing inlet temperature, the $\overline{h}$ increases slightly while the ΔP decreases slightly, which are also found in the simulation results. The main cause for the subtle variations in $\overline{h}$ and ΔP is that the temperature variation affects the physical properties of the water. When the heat flux is 200 W/cm^2, the inlet temperature is 293 K and the inlet mass flow rate is only 28 g/s, the $\overline{\overline{T}}_{heat}$ does not exceed 348 K, while the ΔP is only 2.46 kPa.

To further assess the comprehensive performance of the optimal heat sink in this work, the optimal SJIMHS is compared with the JIMHS in the literature [36,39,52]. The coolant in all the literature compared is water. The average heat transfer coefficient and pumping power to heating power ratio are adopted as the evaluation indexes. The values of the evaluation indexes in the literature are back calculated from the available information. The smaller the pumping power to heating power ratio and the higher the average heat transfer coefficient, the better the comprehensive performance of the heat sink. Generally, heat flux variations may have effects on the curve variation, so the corresponding heat fluxes are marked on the legend. As illustrated in Fig. 23, with the increase of pumping power to heating power ratio, the average heat transfer coefficient will rise simultaneously, indicating that the cooling capacity is improved. Compared with the literature results, the optimal heat sink obtained after multi-objective optimization in this work realizes a significant enhancement in cooling capacity without significantly increasing the pumping power to heating power ratio.

5. Conclusions

The cooling capacity and flow behaviours of the optimal hybrid heat sink, obtained after multi-objective optimization, are evaluated through a series of numerical simulations and experimental measurements. By varying test conditions, the influence of inlet mass flow rate, heat flux and inlet temperature variations on the overall characteristics of the optimal heat sink were assessed. The main conclusions can be summarized as follows.

(1) Comparing the relative errors between simulation results and experimental results under the same working conditions, the maximum relative errors of ΔP and $\overline{\overline{T}}_{heat}$ are both within an acceptable range. Thus, the credibility of the numerical simulation in this work can be verified.

(2) The alternative placement of the inlet and outlet branch passages results in alternating rows of high and low temperature regions on the heated surface. Moreover, the inlet fluid splash and uneven pressure distribution along the inlet branch passage lead to uneven mass flow distribution among microchannels. The closer to the ends of the inlet or outlet branch passages, the corresponding mass flow rate in the microchannels is higher.

(3) As the inlet velocity rises, the downtrend of $\overline{\overline{T}}_{trans}$ and $\overline{\overline{T}}_{heat}$ is dwindled, while the uptrend of ΔP is accelerated. Therefore, for liquid forced cooling, it is unwise to rely on increased inlet mass flow rates to further improve the heat transfer performance at high mass flow rate. In this situation, increasing the inlet mass flow rate provides limited improvement on heat transfer performance, but will result in a significant deterioration in flow resistance performance.

(4) According to the experimental results, when the heat flux is 200 W/cm^2, the inlet mass flow rate is 28 g/s and the inlet temperature is 293 K, the $\overline{\overline{T}}_{heat}$ does not exceed 348 K, while the ΔP is only 2.46 kPa. Additionally, compared with the literature results, the optimal heat sink obtained after multi-objective optimization achieves a significant enhancement in cooling capacity, while the pumping power to heating power ratio is not significantly increased.

Declaration of competing interest

The authors declared that there is no conflict of interest.

Data availability

Data will be made available on request.

Acknowledgement

This work was supported by the National Natural Science Foundation of China (grant no. 51736004).

References

[1] X. Feng, Y. Jiang, X. Yang, M. Du, X. Li, Computer vision algorithms and hardware implementations: a survey, Integration 69 (2019) 309–320.
[2] V. Kakani, V.H. Nguyen, B.P. Kumar, H. Kim, V.R. Pasupuleti, A critical review on computer vision and artificial intelligence in food industry, Journal of Agriculture and Food Research 2 (2020), 100033.
[3] C. Shan, C. Weng, G. Wang, D. Su, M. Luo, D. Yu, L. Xie, Component fusion: learning replaceable language model component for end-to-end speech recognition system, in: ICASSP 2019 - 2019 IEEE International Conference on Acoustics, Speech and Signal Processing, ICASSP), 2019, pp. 5361–5635.
[4] A. Amberkar, P. Awasarmol, G. Deshmukh, P. Dave, Speech recognition using recurrent neural networks, in: International Conference on Current Trends towards Converging Technologies, vol. 2018, ICCTCT), 2018, pp. 1–4.
[5] A. Galassi, M. Lippi, P. Torroni, Attention in natural language processing, IEEE Transact. Neural Networks Learn. Syst. 32 (2021) 4291–4308.
[6] S. Deng, H. Zhao, W. Fang, J. Yin, S. Dustdar, A.Y. Zomaya, Edge intelligence: the confluence of edge computing and artificial intelligence, IEEE Internet Things J. 7 (2020) 7457–7469.
[7] A. Krizhevsky, I. Sutskever, G.E. Hinton, ImageNet classification with deep convolutional neural networks, Commnications of the ACM 60 (2017) 84–90.
[8] T. Brown, B. Mann, N. Ryder, M. Subbiah, J.D. Kaplan, P. Dhariwal, A. Neelakantan, P. Shyam, G. Sastry, A. Askell, Language models are few-shot learners, Adv. Neural Inf. Process. Syst. 33 (2020) 1877–1901.

[9] A. Lohn, M. Musser, How much longer can computing power, drive artificial intelligence progress?. https://cset.georgetown.edu/wp-content/uploads/AI-and-Compute-How-Much-Longer-Can-Computing-Power-Drive-Artificial-Intelligence-Progress_v2.pdf, 2022.

[10] A.D. Franklin, Nanomaterials in transistors: from high-performance to thin-film applications, Science 349 (2015) aab2750.

[11] A. Bar-Cohen, J.J. Maurer, J.G. Felbinger, DARPA's intra/interchip enhanced cooling (ICECool) program, in: CS MANTECH Conference, 2013. May 13th-16th.

[12] I. Mudawar, Assessment of high-heat-flux thermal management schemes, IEEE Trans. Compon. Packag. Technol. 24 (2001) 122–141.

[13] S.N. Li, H.N. Zhang, J.P. Cheng, X.B. Li, W.H. Cai, Z.Y. Li, F.C. Li, A state-of-the-art overview on the developing trend of heat transfer enhancement by single-phase flow at micro scale, Int. J. Heat Mass Tran. 143 (2019), 118476.

[14] F. Pourfattah, A.A.A. Arani, M.R. Babaie, H.M. Nguyen, A. Asadi, On the thermal characteristics of a manifold microchannel heat sink subjected to nanofluid using two-phase flow simulation, Int. J. Heat Mass Tran. 143 (2019), 118518.

[15] D.B. Tuckerman, R.F.W. Pease, High-performance heat sinking for VLSI, IEEE Electron. Device Lett. 2 (1981) 126–129.

[16] H. Shen, H. Liu, X. Shao, G. Xie, C.-C. Wang, Thermofluids performances on innovative design with multi-circuit nested loop applicable for double-layer microchannel heat sinks, Appl. Therm. Eng. 219 (2023), 119699.

[17] H. Shen, G. Xie, C.-C. Wang, H. Liu, Experimental and numerical examinations of thermofluids characteristics of double-layer microchannel heat sinks with deflectors, Int. J. Heat Mass Tran. 182 (2022), 121961.

[18] H. Shen, G. Xie, C.-C. Wang, Heat transfer and thermodynamic analysis by introducing multiple alternation structures into double-layer microchannel heat sinks, Int. J. Therm. Sci. 145 (2019), 105975.

[19] Y. Hadad, B. Ramakrishnan, R. Pejman, S. Rangarajan, P.R. Chiarot, A. Pattamatta, B. Sammakia, Three-objective shape optimization and parametric study of a micro-channel heat sink with discrete non-uniform heat flux boundary conditions, Appl. Therm. Eng. 150 (2019) 720–737.

[20] H.A. Kose, A. Yildizeli, S. Cadirci, Parametric study and optimization of microchannel heat sinks with various shapes, Appl. Therm. Eng. 211 (2022), 118368.

[21] M. Magnini, O.K. Matar, Numerical study of the impact of the channel shape on microchannel boiling heat transfer, Int. J. Heat Mass Tran. 150 (2020), 119322.

[22] R. A, S. Chakraborty, Effect of shape and arrangement of micro-structures in a microchannel heat sink on the thermo-hydraulic performance, Appl. Therm. Eng. 190 (2021), 116755.

[23] R. A, S. Chakraborty, Effect of micro-structures in a microchannel heat sink – a comprehensive study, Int. J. Heat Mass Tran. 154 (2020), 119617.

[24] M.K. Sung, I. Mudawar, Effects of jet pattern on single-phase cooling performance of hybrid micro-channel/micro-circular-jet-impingement thermal management scheme, Int. J. Heat Mass Tran. 51 (2008) 4614–4627.

[25] R.D. Plant, J. Friedman, M.Z. Saghir, A review of jet impingement cooling, International Journal of Thermofluids 17 (2023), 100312.

[26] H.C. Cui, J.H. Xie, R.Z. Zhao, M.Z. Wang, Z.C. Liu, W. Liu, Thermal-hydraulic performance analysis of a hybrid micro pin-fin, jet impingement heat sink with non-uniform heat flow, Appl. Therm. Eng. 208 (2022), 118201.

[27] A.J. Robinson, A thermal–hydraulic comparison of liquid microchannel and impinging liquid jet array heat sinks for high-power electronics cooling, IEEE Trans. Compon. Packag. Technol. 32 (2009) 347–357.

[28] P. McInturff, M. Suzuki, P. Ligrani, C. Nakamata, D.H. Lee, Effects of hole shape on impingement jet array heat transfer with small-scale, target surface triangle roughness, Int. J. Heat Mass Tran. 127 (2018) 585–597.

[29] D. Singh, B. Premachandran, S. Kohli, Effect of nozzle shape on jet impingement heat transfer from a circular cylinder, Int. J. Therm. Sci. 96 (2015) 45–69.

[30] E.N. Wang, L. Zhang, L.N. Jiang, J.M. Koo, J.G. Maveety, E.A. Sanchez, K. E. Goodson, T.W. Kenny, Micromachined jets for liquid impingement cooling of VLSI chips, J. Microelectromech. Syst. 13 (2004) 1072, 1072.

[31] M. Sabato, A. Fregni, E. Stalio, F. Brusiani, M. Tranchero, T. Baritaud, Numerical study of submerged impinging jets for power electronics cooling, Int. J. Heat Mass Tran. 141 (2019) 707–718.

[32] X. Du, Z. Yang, H. Zhou, Q. Li, Z. Jin, Numerical Investigation of Geometry Effects on Flow, Heat Transfer and Defrosting Characteristics of a Simplified Automobile Windshield with a Single Row of Impinging Jets, SAE Technical Paper, 2016, pp. 148–7191.

[33] A.J. Robinson, E. Schnitzler, An experimental investigation of free and submerged miniature liquid jet array impingement heat transfer, Exp. Therm. Fluid Sci. 32 (2007) 1–13.

[34] M.K. Sung, I. Mudawar, Single-phase and two-phase cooling using hybrid micro-channel/slot-jet module, Int. J. Heat Mass Tran. 51 (2008) 3825–3839.

[35] M.K. Sung, I. Mudawar, Single-phase and two-phase heat transfer characteristics of low temperature hybrid micro-channel/micro-jet impingement cooling module, Int. J. Heat Mass Tran. 51 (2008) 3882–3895.

[36] Z. Deng, J. Shen, W. Dai, Y.W. Liu, Q.L. Song, W.C. Gong, L. Ke, M.Q. Gong, Flow and thermal analysis of hybrid mini-channel and slot jet array heat sink, Appl. Therm. Eng. 171 (2020), 115063.

[37] A. Husain, M. Ariz, N.Z.H. Al-Rawahi, M.Z. Ansari, Thermal performance analysis of a hybrid micro-channel, -pillar and -jet impingement heat sink, Appl. Therm. Eng. 102 (2016) 989–1000.

[38] X.M. Huang, W. Yang, T.Z. Ming, W.Q. Shen, X.F. Yu, Heat transfer enhancement on a microchannel heat sink with impinging jets and dimples, Int. J. Heat Mass Tran. 112 (2017) 113–124.

[39] W. Gao, J.F. Zhang, Z.G. Qu, W.Q. Tao, Numerical investigations of heat transfer in hybrid microchannel heat sink with multi-jet impinging and trapezoidal fins, Int. J. Therm. Sci. 164 (2021), 106902.

[40] M. Peng, L. Chen, W. Ji, W. Tao, Numerical study on flow and heat transfer in a multi-jet microchannel heat sink, Int. J. Heat Mass Tran. 157 (2020), 119982.

[41] C.U. Gonzalez-Valle, S. Samir, B. Ramos-Alvarado, Experimental investigation of the cooling performance of 3-D printed hybrid water-cooled heat sinks, Appl. Therm. Eng. 168 (2020), 114823.

[42] T.W. Wei, H. Oprins, V. Cherman, G. Van der Plas, I. De Wolf, E. Beyne, M. Baelmans, Experimental characterization and model validation of liquid jet impingement cooling using a high spatial resolution and programmable thermal test chip, Appl. Therm. Eng. 152 (2019) 308–318.

[43] T.W. Wei, H. Oprins, L. Fang, V. Cherman, I. De Wolf, E. Beyne, M. Baelmans, Nozzle scaling effects for the thermohydraulic performance of microjet impingement cooling with distributed returns, Appl. Therm. Eng. 180 (2020), 115767.

[44] R. Wu, Y. Fan, T. Hong, H. Zou, R. Hu, X. Luo, An immersed jet array impingement cooling device with distributed returns for direct body liquid cooling of high power electronics, Appl. Therm. Eng. 162 (2019), 114259.

[45] A.J. Robinson, R. Kempers, J. Colenbrander, N. Bushnell, R. Chen, A single phase hybrid micro heat sink using impinging micro-jet arrays and microchannels, Appl. Therm. Eng. 136 (2018) 408–418.

[46] H.C. Cui, C.Y. Shi, M.J. Yu, Z.K. Zhang, Z.C. Liu, W. Liu, Optimal parameter design of a slot jet impingement/microchannel heat sink base on multi-objective optimization algorithm, Appl. Therm. Eng. 227 (2023), 120452.

[47] S.N. Joshi, E.M. Dede, Effect of sub-cooling on performance of a multi-jet two phase cooler with multi-scale porous surfaces, Int. J. Therm. Sci. 87 (2015) 110–120.

[48] F. Zhou, E.M. Dede, S.N. Joshi, Ieee, A novel design of hybrid slot jet and mini-channel cold plate for electronics cooling, in: 31st Annual Semiconductor Thermal Measurement, Modeling and Management Symposium (SEMI-THERM), 2015, pp. 60–67. San Jose, CA.

[49] F. Zhou, Y. Liu, Y.H. Liu, S.N. Joshi, E.M. Dede, Modular design for a single-phase manifold mini/microchannel cold plate, J. Therm. Sci. Eng. Appl. 8 (2016), 021010.

[50] G. Zhou, J. Li, Z. Jia, Power-saving exploration for high-end ultra-slim laptop computers with miniature loop heat pipe cooling module, Appl. Energy 239 (2019) 859–875.

[51] R. van Erp, R. Soleimanzadeh, L. Nela, G. Kampitsis, E. Matioli, Co-designing electronics with microfluidics for more sustainable cooling, Nature 585 (2020) 211–216.

[52] Y.J. Zhang, S.F. Wang, P.X. Ding, Effects of channel shape on the cooling performance of hybrid micro-channel and slot-jet module, Int. J. Heat Mass Tran. 113 (2017) 295–309.